

Density Fluctuations in the Intracluster Medium: An Attempt to Constrain Viscosity with Cosmological Simulations

TIRSO MARIN-GILABERT ¹, ULRICH P. STEINWANDEL ², MILENA VALENTINI ^{3,4,5,6}, DAVID VALLÉS-PÉREZ ⁷ AND
KLAUS DOLAG^{1,8}

¹*Universitäts-Sternwarte, Fakultät für Physik, Ludwig-Maximilians-Universität München, Scheinerstr.1, 81679 München, Germany*

²*Center for Computational Astrophysics, Flatiron Institute, 162 5th Avenue, New York, NY 10010*

³*Astronomy Unit, Department of Physics, University of Trieste, via Tiepolo 11, I-34131 Trieste, Italy*

⁴*INAF - Osservatorio Astronomico di Trieste, via Tiepolo 11, I-34131 Trieste, Italy*

⁵*INFN, Istituto Nazionale di Fisica Nucleare, Via Valerio 2, I-34127, Trieste, Italy*

⁶*ICSC - Italian Research Center on High Performance Computing, Big Data and Quantum Computing, via Magnanelli 2, 40033, Casalecchio di Reno, Italy*

⁷*Departament d'Astronomia i Astrofísica, Universitat de València, C/Doctor Moliner 50, E-46100 Burjassot (València), Spain*

⁸*Max-Planck-Institut für Astrophysik, Karl-Schwarzschild-Straße 1, 85741 Garching, Germany*

(Received July 16, 2024; Revised September 25, 2024; Accepted September 28, 2024)

Submitted to ApJ

ABSTRACT

The impact of viscosity in the Intracluster Medium (ICM) is still an open question in astrophysics. To address this problem, we have run a set of cosmological simulations of three galaxy clusters with a mass larger than $M_{\text{vir}} > 10^{15} M_{\odot}$ at $z = 0$ using the SPMHD-code `OPENGADGET3`. We aim to quantify the influence of viscosity and constrain its value in the ICM. Our results show significant morphological differences at small scales, temperature variations, and density fluctuations induced by viscosity. We observe a suppression of instabilities at small scales, resulting in a more filamentary structure and a larger amount of small structures due to the lack of mixing with the medium. The conversion of kinetic to internal energy leads to an increase of the virial temperature of the cluster of $\sim 5\% - 10\%$, while the denser regions remain cold. The amplitude of density and velocity fluctuations are found to increase with viscosity. However, comparison with observational data indicates that the simulations, regardless of the viscosity, match the observed slope of the amplitude of density fluctuations, challenging the direct constraint of viscosity solely through density fluctuations. Furthermore, the ratio of density to velocity fluctuations remains close to 1 regardless of the amount of viscosity, in agreement with the theoretical expectations. Our results show for the first time in a cosmological simulation of a galaxy cluster the effect of viscosity in the ICM, a study that is currently missing in the literature.

Keywords: Computational methods(1965) — Intracluster medium(858) — Galaxy clusters(584) — Magnetohydrodynamical simulations(1966)

1. INTRODUCTION

The Intracluster Medium (ICM) is the dominant baryonic component visible in galaxy clusters, filling the gravitational potential with hot ($T \sim 10^7 - 10^8$ K) ionised, X-ray emitting gas. This gas is continually perturbed by galaxy motions (e.g. Faltenbacher et al. 2005),

mergers (e.g. ZuHone 2011; Iapichino et al. 2017), AGN outflows (e.g. O'Neill et al. 2009; Gaspari 2015) and accretion of gas along filaments (e.g. Kravtsov & Borgani 2012; Vallés-Pérez et al. 2021a). These processes inject energy at large scales (low wavenumber k), which decays towards higher k modes in a Kolmogorov-like cascade, introducing turbulence on a wide range of scales (e.g. Kolmogorov 1941, 1962). The energy is then dissipated into heat, affecting small scale processes such as cosmic

ray re-acceleration (e.g. Fujita et al. 2003; Brunetti & Lazarian 2007), star formation (e.g. Federrath 2016) or magnetic field amplification (e.g. Kazantsev 1968; Kulsrud & Anderson 1992). These complex mechanisms over cosmological periods of time produce very complicated scenarios in which the transport properties of the gas are fundamental.

Probing the turbulent nature of the ICM via observations is crucial for understanding the gas dynamics and, therefore, the physics and gas properties of the cluster (Gilfanov et al. 1987; Churazov et al. 2004). The Hitomi collaboration (Aharonian et al. 2018) measured subsonic speeds of the gas with a 3D mach number of $\mathcal{M}_{3D} \sim 0.3 - 0.45$ in Perseus. However, with the exception of the Hitomi collaboration, direct measurements of velocities are not available yet (although they soon will be with the launch of *XRISM* in 2023, a high-resolution X-ray spectrometer, *XRISM Science Team* 2020). Therefore, indirect measurements are needed to infer the dynamics of the gas. This can be done by measuring the X-ray surface brightness and pressure fluctuations (Soltan & Fabricant 1990; Schuecker et al. 2004; Churazov et al. 2012) and linking them to density fluctuations induced by turbulence. Zhuravleva et al. (2014) showed theoretically that subsonic gas motions driven on large scales in a stratified atmosphere can introduce density fluctuations. The amplitude of these density fluctuations is expected to scale linearly with the amplitude of the one-component velocity fluctuations at each scale (Zhuravleva et al. 2014).

This relation has been tested in galaxy cluster simulations, where Zhuravleva et al. (2014) found a proportionality coefficient between density and velocity amplitude fluctuations of $\eta_\rho \approx 1.0 \pm 0.3$, as predicted theoretically, and Gaspari et al. (2014) a value of $\eta_\rho \approx 1.3$. Using cosmological simulations of galaxy cluster formation, Simonte et al. (2022) found that this relation depends on the dynamical state of the cluster, with $\eta_\rho \approx 1.15 \pm 0.06$ for relaxed clusters, but a flatter relation and a larger dispersion for unrelaxed clusters persists. The importance of the dynamical state was tested in Zhuravleva et al. (2023), showing that relaxed clusters tend to have a proportionality coefficient closer to 1 than unrelaxed clusters, where the coefficient tends to be larger. This is because in unrelaxed clusters, the assumption of a nearly hydrostatic atmosphere does not hold anymore, producing a larger scatter in the density-velocity fluctuations. Zhuravleva et al. (2023) also showed that accounting for halo ellipticity might be important, especially for the inner regions of relaxed clusters. The density-velocity fluctuations relation is not universal, but depends on the level of stratification, characterized by the Richard-

son number Ri ¹. Mohapatra et al. (2020) found that η_ρ increases with Ri , ranging from $0.01 \lesssim \eta_\rho^2 \lesssim 1$ for Ri from 0 to 10.

The properties of these density perturbations do not only reflect the driving mechanisms that trigger them, but also depend on the microphysics of the ICM, specifically, for thermal conduction (Ruszkowski et al. 2011) and viscosity (Zhuravleva et al. 2019; Kunz et al. 2022). Zhuravleva et al. (2019) suggested to use observations of density fluctuations to constrain the amount of viscosity in galaxy clusters. The idea is to compare the amplitude of density fluctuations measured in observations against simulations with different amounts of viscosity. Using Coma observations and simulations of incompressible hydrodynamic turbulence carried out using Direct Numerical Simulations (DNS), Zhuravleva et al. (2019) concluded that the effective isotropic viscosity must be suppressed by at least a factor of ~ 10 to ~ 1000 with respect to the Spitzer value. This suppression could be the effect of magnetic fields, which reduce the effect of viscosity (ZuHone et al. 2015; Berlok et al. 2019; Squire et al. 2023), as well as an enhanced scattering rate due to plasma instabilities (Schekochihin & Cowley 2006; Kunz et al. 2014; Berlok et al. 2021).

The physics of the ICM has been studied extensively using simulations of isolated systems with more idealised setups (e.g. ZuHone et al. 2009; Brüggén et al. 2012; Mohapatra et al. 2020; Zhang et al. 2020) and cosmological simulations (e.g. Dolag et al. 2005; Teyssier et al. 2011; Vazza et al. 2016; Pakmor et al. 2023; Steinwandel et al. 2024). Similarly, viscosity in the context of ICM has also been extensively studied with simulations, focusing on its effect on AGN-powered bubbles (Scannapieco & Brüggén 2008; Dong & Stone 2009), on the suppression of instabilities in cold fronts (Roediger & ZuHone 2011; Suzuki et al. 2013; ZuHone et al. 2015) and on its impact on stripped galaxies (Roediger et al. 2015; Kraft et al. 2017).

However, viscosity in the intracluster medium (ICM) has not been extensively studied using cosmological simulations. The only study in the literature, by Sijacki & Springel (2006), did not provide a detailed analysis of these effects. In our study, we conduct a set of cosmological simulations focusing on how viscosity affects massive clusters in a realistic scenario. We use different values of the isotropic Spitzer viscosity (Spitzer 1962; Braginskii 1965) and compare it with the non-viscous case. Our goal is to provide a general view of how the morphology

¹ On large scales, stratification is expected to be dominant over turbulence ($Ri > 1$), while on small scales turbulence dominates ($Ri < 1$) (Mohapatra et al. 2020).

of the cluster is affected by viscosity and how the virial temperature depends on the amount of viscosity. We also want to test the criteria to constrain viscosity suggested by [Zhuravleva et al. \(2019\)](#) and if this criterion holds in the context of the complex, realistic cosmological simulation. To this end, we compare our results with observations of density fluctuations from [Heinrich et al. \(2024\)](#). Additionally, we want to verify if the density fluctuations scale linearly with the velocity fluctuations, independently of the how viscous the ICM is. Although full Spitzer viscosity is larger than expected, due to the different mechanisms that suppress the viscous stress, we want to show this extreme case for a better understanding of the ongoing mechanisms. In a follow up work, we will show additional consequences of a viscous ICM such as changes of the magnetic field amplification, effects in the merger history or the different energy distribution, together with the time evolution of gas properties.

This paper is organised as follows. In Sec. 2 we introduce the relevant equations and our setup. In Sec. 3 we show the results obtained from our simulations and the comparison with observations. Finally, we discuss the results obtained and conclude in Sec. 4.

2. METHODS

2.1. Theoretical considerations

The ICM can be understood as a compressible magnetised plasma, therefore it can be described using the equations of magnetohydrodynamics (MHD):

$$\frac{d\rho}{dt} + \rho \nabla \cdot \mathbf{v} = 0, \quad (1)$$

$$\rho \frac{d\mathbf{v}}{dt} + \nabla P = -\rho \nabla \Phi - \nabla \cdot \mathbf{\Pi} + \frac{(\nabla \times \mathbf{B}) \times \mathbf{B}}{4\pi}, \quad (2)$$

$$\begin{aligned} \frac{dE}{dt} + \mathbf{v} \cdot \nabla P + (E + P) \nabla \cdot \mathbf{v} - \nabla \cdot \frac{\mathbf{B}(\mathbf{v} \cdot \mathbf{B})}{4\pi} = \\ -\rho \mathbf{v} \cdot \nabla \Phi - \nabla \cdot \mathbf{Q} - \nabla \cdot (\mathbf{\Pi} \cdot \mathbf{v}) \end{aligned} \quad (3)$$

$$\frac{\partial \mathbf{B}}{\partial t} = \nabla \times (\mathbf{v} \times \mathbf{B}), \quad (4)$$

where

$$\frac{d}{dt} = \frac{\partial}{\partial t} + (\mathbf{v} \cdot \nabla) \quad (5)$$

is the Lagrangian derivative. ρ is the gas density, \mathbf{v} the velocity of the fluid, \mathbf{B} the magnetic field, \mathbf{Q} is the heat flux and Φ is the gravitational potential. E is the energy per unit volume (kinetic + thermal + magnetic)

$$E = \frac{\rho \mathbf{v}^2}{2} + \rho u + \frac{\mathbf{B}^2}{8\pi}, \quad (6)$$

with u being the specific internal energy. P is the pressure

$$P = (\gamma - 1)\rho u, \quad (7)$$

with an adiabatic index of $\gamma = 5/3$ for monoatomic gases. $\mathbf{\Pi}$ is the viscous stress tensor, which defines the behaviour of Spitzer viscosity as

$$\mathbf{\Pi} = \eta \sigma_{ij} = \eta \left(\frac{\partial v_i}{\partial x_j} + \frac{\partial v_j}{\partial x_i} - \frac{2}{3} \delta_{ij} \frac{\partial v_k}{\partial x_k} \right), \quad (8)$$

where we have dropped the bulk viscosity term, since it is related to the degrees of freedom of molecular rotations, being zero for monoatomic gases (see e.g [Zeldovich & Raizer 1967](#); [Pitaevskii & Lifshitz 1981](#)). The viscous stress tensor is equal to the rate of strain tensor (σ_{ij}) multiplied by the shear viscosity coefficient η , defined as

$$\eta = 0.406 \frac{m_i^{1/2} (k_B T_i)^{5/2}}{(Ze)^4 \ln \Lambda}, \quad (9)$$

where m_i is the mass of the proton, T_i is the temperature of the plasma, Ze is the ion charge and $\ln \Lambda$ is the Coulomb logarithm.

Assuming subsonic gas motions within the galaxy cluster ($v \ll c_s$) and a stratified atmosphere, density perturbations are expected to be proportional to the one-component velocity at each scale $l = 1/k$

$$\left(\frac{\delta \rho}{\rho} \right)_k^2 = \eta_\rho^2 \left(\frac{v_{1D}}{c_s} \right)_k^2 = \eta_\rho^2 \mathcal{M}_{1D,k}^2. \quad (10)$$

c_s is the soundspeed of the medium and $\mathcal{M}_{1D,k}$ the 1D mach number. A complete derivation can be found in [Zhuravleva et al. \(2014\)](#).

2.2. Viscosity saturation

A proper treatment of viscosity requires the implementation of a viscosity saturation to avoid unphysical results. The viscous stress saturates when the scale over which the velocity varies becomes smaller than the ion mean free path. This means that the viscous momentum transfer propagates faster than the mean soundspeed of the medium, overestimating this momentum transfer ([Sarazin 1986](#)).

To avoid this, we need to introduce a viscosity saturation that limits the momentum propagation and ensures a smooth transition from the non-saturated to the saturated state. We do this in such a way that the momentum transfer of the saturated viscosity propagates at a velocity comparable to the soundspeed of the medium. We define the velocity length scale as $l_v = 2c_s/|\sigma_{ij}|$, where

$$|\sigma_{ij}| = \sqrt{\text{tr}(\sigma_{ij}^2)} = \sqrt{\text{tr}(\sigma_{ij} \cdot \sigma_{ij})} = \sqrt{\text{tr}(\sigma_{xx}^2 + \sigma_{yy}^2 + \sigma_{zz}^2 + 2\sigma_{xy}^2 + 2\sigma_{xz}^2 + 2\sigma_{yz}^2)} \quad (11)$$

is the strength of the rate of strain tensor of the viscous stress tensor. We now introduce the viscosity saturation as the analogous to the thermal conduction saturation (Cowie & McKee 1977), following the implementation done in Su et al. (2017):

$$\eta_{\text{Sat}} = \frac{\eta}{1 + 4.2 \frac{\lambda_I}{l_v}}, \quad (12)$$

where λ_I is the ion mean free path:

$$\lambda_I = \frac{3^{3/2}(k_B T_I)^2}{4\pi^{1/2} n_I e^4 \ln \Lambda}. \quad (13)$$

Here, T_I is the ion temperature, n_I the ion number density, e the electric charge and $\ln \Lambda = 37.8$ the Coulomb logarithm. This way we make sure that when $l_v < \lambda_I$, the shear viscosity coefficient saturates, avoiding unphysical large values of the viscous stress tensor $\mathbf{\Pi}$ and numerical issues like extremely small timesteps.

2.3. Simulation Setup

We perform cosmological, magneto-hydrodynamical simulations of galaxy clusters using the smoothed particle magneto-hydrodynamics (SPMHD) code OPENGADGET3 (Springel 2005; Groth et al. 2023). Gravity is solved via the Tree-PM method, where the long-distance gravitational forces are computed on a PM mesh and the short-distance forces are computed on a gravity tree. For the hydro computation we used the modern SPH implementation (Beck et al. 2016), including artificial viscosity (Balsara 1995; Cullen & Dehnen 2010) and artificial conductivity (Price 2008), with a Wendland C^6 kernel (Wendland 1995; Dehnen & Aly 2012) and 295 neighbours. This is necessary to avoid the ‘pairing instability’ (Price 2012) and the ‘ E_0 error’ (Read et al. 2010) and capture mixing properly (Tricco & Price 2013; Hu et al. 2014).

We also include magnetic fields based on the implementation of Bonafede et al. (2011) and Stasyszyn et al. (2013), with an initial seed of $B_{\text{seed}} = 10^{-12}$ G (comoving) in the x -direction, which corresponds to an initial magnetic field of $B_{\text{ini,ph}} = B_{\text{seed}} \cdot (1 + z_{\text{ini}})^2 = 1.98 \times 10^{-8}$ G in physical units. The choice of this initial magnetic field leads to a saturation of the dynamo at $z \sim 1.5$ at this resolution (Steinwandel et al. 2022, Marin-Gilabert et al, in prep). Our simulations also include anisotropic thermal conductivity via a bi-conjugate gradient solver (Arth et al. 2017; Steinwandel et al. 2022).

To properly understand the effects of physical viscosity, we perform three different simulations for each

cluster: one with no viscosity (labeled as “Ideal”), one with 1/3 of Spitzer viscosity (labeled as “1/3 η ”) and one with full Spitzer viscosity (labeled as “ η ”). The implementation of viscosity in OPENGADGET3 is described in Sijacki & Springel (2006) and Marin-Gilabert et al. (2022). Now, we additionally include a viscous saturation (see section 2.2 for details) to avoid unphysical results (Cowie & McKee 1977; Sarazin 1986; Su et al. 2017). On top of the physical viscosity, a higher order shock capturing method (i.e. artificial viscosity) is necessary to properly capture shocks in SPH (Monaghan & Gingold 1983; Monaghan 1992) even when physical viscosity is implemented (Sijacki & Springel 2006).

We want to focus on understanding the complex properties of gas in the ICM, in particular the effect of viscosity and its observational implications. For this reason, we run non-radiative simulations without the effects of subgrid models (e.g. star formation and feedback).

2.4. Initial Conditions

We ran a total of nine zoom-in simulations of three different galaxy clusters from the Dianoga suite (Bonafede et al. 2011; Ragone-Figueroa et al. 2013): the g5503149, g1657050 and g6348555 regions (labeled as g55, g16 and g63, respectively) at the 10x resolution level. These clusters were taken from a low-resolution N -body cosmological simulation of a periodic box of $1 h^{-1}$ Gpc comoving size. Each Lagrangian region was then re-simulated with a higher resolution using the *zoomed initial conditions technique* (Tormen et al. 1997).

We chose the g55, g16 and g63 clusters because they have a $M_{\text{Vir}}^2 > 10^{15} M_{\odot}$ at $z = 0$; g55 and g16 are expected to be unrelaxed, while g63 is very relaxed. To classify the clusters as relaxed or unrelaxed, we used the centre-of-mass offset, where we measured the separation between the density peak position and the center of mass within R_{200c} (Power et al. 2012; Cui et al. 2016). The adopted cosmological parameters are $\Omega_0 = 0.24$, $\Omega_{\Lambda} = 0.76$, $\Omega_b = 0.04$, $h = 0.72$ and $\sigma_8 = 0.8$. The initial redshift for all the simulations is $z_{\text{ini}} = 140$ and the mass resolution is $m_{\text{gas}} = 1.56 \times 10^7 M_{\odot}$ in gas particles and $m_{\text{dm}} = 8.44 \times 10^7 M_{\odot}$ in dark matter. The choice of this particle resolution is due to the convergence in the magnetic field amplification shown in Steinwandel et al. (2022) against a lower particle resolution. The details of each cluster at $z = 0$ are shown in table 1.

3. RESULTS

² The suffix *Vir* indicates the virialized gas, i.e. the gas within the galaxy cluster that satisfies the virial theorem.

Table 1. Properties of the three different clusters used in this work with three different amounts of viscosity. First column shows the virial mass, second column the virial temperature, third column the R_{2500c} and fourth column shows R_{200c} , each at $z = 0$.

	$M_{\text{Vir}} [10^{15} M_{\odot}]$			$T_{\text{Vir}} [\text{K}]$			$R_{2500c} [\text{kpc}]$			$R_{200c} [\text{kpc}]$		
	Ideal	1/3 η	η	Ideal	1/3 η	η	Ideal	1/3 η	η	Ideal	1/3 η	η
g55	1.34	1.38	1.33	7.05×10^7	7.32×10^7	7.39×10^7	498.21	509.77	510.40	3000.96	3020.54	2995.14
g16	1.44	1.40	1.20	6.22×10^7	6.29×10^7	6.22×10^7	459.07	460.04	435.29	3232.38	3204.37	3086.66
g63	1.11	1.22	1.17	6.40×10^7	7.81×10^7	6.91×10^7	455.19	499.39	471.84	2939.73	3019.53	2976.75

In this section we present the results obtained from the three different clusters and the three different values of viscosity employed. We focus first on the intrinsic effect of viscosity with respect to the non-viscous case and then we will try to constrain the viscosity from X-ray observations.

3.1. Morphology

Viscosity acts by transforming kinetic energy into internal energy, leading to a suppression of the growth of hydrodynamical instabilities and to an increase of the gas temperature (Roediger et al. 2013; Marin-Gilabert et al. 2022). This is expected to produce a strong effect in the morphology of galaxy clusters at small scales (few kpc), where the turbulent cascade is truncated due to the effect of viscosity. Fig. 1 shows the surface density for each of the three clusters and the three different configurations. The inner dotted circle corresponds to R_{2500c} and the outer dashed circle corresponds to R_{200c} ³.

By comparing each cluster independently, we can observe that there are no major changes at large scales (few hundred kpc - Mpc), where the big structures remain in the same position in the three different cases and the overall gas distribution is very similar. However, the ICM is more homogeneous in the non-viscous case, whereas in the viscous cases we find sharper density discontinuities and more regions with very diffuse gas.

Although at large scale the picture is similar, we find many differences at smaller scales. The lack of mixing due to viscosity leads to more small structures that have not been disrupted due to the growth of instabilities. The survival of the clump will depend on different parameters such as the size of the clump, its velocity or the overdensity with respect to the medium (Klein et al. 1994; Pittard et al. 2005; Valentini & Brighenti 2015), which is beyond of the scope of this paper. The

growth or suppression of instabilities will also depend on the amount of viscosity, which depends on the temperature, generating a very complex system difficult to analyse in cosmological simulations. However, its effect can be seen in the amount of clumps observed in Fig. 1.

Another morphological difference observed in the cases with viscosity is the filamentary structure. This is produced by the infalling structures moving towards the center of the cluster, which experience a ram pressure stripping (e.g. Gisler 1976; Nusen 1982; Randall et al. 2008). This stripped gas produces a tail with a density contact discontinuity with respect to the medium, resulting in the growth of instabilities. Viscosity slows down the growth process of these instabilities, leading to longer tails that last for longer periods of time (Roediger et al. 2015; Kraft et al. 2017). Although magnetic fields can also produce these filamentary structures (Das & Gronke 2023), all our simulations include magnetic fields, excluding it as the origin of these differences.

Because of the strong dependence of viscosity with temperature one might expect that the above-mentioned differences might correlate well with the temperature of the cluster. In Fig. 2 we show temperature colormaps of the nine different simulations. The cases with more viscosity lead to higher temperatures in the diffuse gas, however, the temperatures of the dense clumps are very similar in all three cases. Overall, the virial temperature at $z = 0$ is around 5% to 10% higher in the viscous cases compared to the ideal ones due to heat dissipation (see table 1). We find again a more homogeneous temperature in the ideal runs, while more fluctuations are present in the viscous runs. Due to the dependence of viscosity on temperature, viscosity starts to become important at low redshift, when the virial temperature becomes larger than $\sim 10^7$ K. In this respect, the merger history of the cluster becomes very important, as mergers behave differently whether we have or we do not have viscosity. This is analysed in full depth in a follow up work. The hotter medium leads to a larger viscosity, which heats up the medium, producing a larger viscosity, entering a runaway cycle which is prevented by the vis-

³ In this paper, R_{2500c} (R_{200c}) is defined as the radius enclosing the region of the cluster with a mean density 2500 (200) times larger than the critical density of the universe.

cous saturation, avoiding unphysical temperatures (see section 2.2).

3.2. Density and velocity fluctuations

3.2.1. Gas distribution

Quantifying the density fluctuations observed in Fig. 1 is fundamental for understanding the small scale processes which determine the ICM properties. Comparing with observations can help us to constrain the amount of viscosity in the ICM, as suggested in Zhuravleva et al. (2019). To this end, we first remove the high-density clumps, leaving only the bulk gas (source of the X-ray emission in the ICM), and then compute the density and velocity fluctuations.

To remove the high-density regions we follow the method introduced in Zhuravleva et al. (2012): we divide the galaxy cluster into spherical shells and compute the density PDF for each of the shells. We calculate the median value of each shell and, alongside it, a threshold value to separate the bulk gas from the high-density gas. A particle is considered to belong to the high-density gas if the following criterion is met:

$$\log_{10} n > \log_{10}\{n\} + f_{\text{cut}}\sigma_{10}, \quad (14)$$

where $\{n\}$ is the median value of the density in the shell, f_{cut} is a parameter tuned to select more or less gas as high-density and σ_{10} is the standard deviation (\log_{10} based) assuming a log-normal distribution of the density PDF. σ_{10} can be expressed as

$$\sigma_{10} = \frac{W_{10}}{2\sqrt{2\ln 2}}, \quad (15)$$

with

$$W_{10}(n) = \log_{10} \frac{n_2}{n_1}. \quad (16)$$

W_{10} accounts for the logarithmic interval where 76% of the particles are contained, n_1 corresponds to the 12th percentile of density and n_2 to the 88th percentile. The value of f_{cut} is set to be between 2.5 and 4.5 (Zhuravleva et al. 2012). A lower value will displace the threshold towards lower densities, selecting a larger number of particles as high-density gas, while a higher value will displace it towards larger densities. We choose a value of $f_{\text{cut}} = 2.5$ for our analysis. The reason for this choice can be seen in Fig. 3. This figure shows the effect of viscosity in the density distribution within a thin shell of 5 kpc around the virial radius of the cluster g55. The vertical dashed lines indicate the position of the density threshold to split the distribution into bulk and high-density gas. Once the gas has been separated, we fit the bulk gas to a log-normal distribution, indicated with the dash-dotted lines. Even though the mean value of

the distribution does not change much, viscosity broadens the distribution. This result shows quantitatively what we observed in Fig. 1. Viscosity produces larger density fluctuations, where particles deviate more from the mean value of the density distribution than in the non-viscous case. As a consequence, choosing a larger value of f_{cut} would displace the threshold in the viscous case further towards larger densities, taking particles of the high-density tail as bulk gas. On the other hand, choosing a rather low value of f_{cut} means that we might be underestimating the threshold in the ideal case (see appendix A). For this reason, we take the lowest value suggested by Zhuravleva et al. (2012).

3.2.2. Density fluctuations

Fig. 3, however, only shows a thin slice of cluster g55 to illustrate the effect of viscosity on the gas distribution and the method employed to separate the bulk gas from the high-density gas. To understand the overall effect of viscosity in the whole cluster, Fig. 4 shows the variation of the standard deviation (σ) of the log-normal fit as a function of the radius for the three different clusters. Assuming the bulk gas follows a log-normal distribution, the value of σ can be understood as a density fluctuation measurement (i.e. the width of the distribution), since

$$\frac{\delta\rho}{\rho} = \log_{10} \frac{\rho_2}{\rho_1} = \frac{2\sqrt{2\ln 2}}{\ln 10} \sigma \simeq 1.02\sigma, \quad (17)$$

where, as before, ρ_1 and ρ_2 correspond to the 12th and the 88th percentile of the density, respectively. Increasing the amount of viscosity produces broader distributions for all the shells along the radius, which translates into larger density fluctuations. Overall, with full Spitzer viscosity we get the largest fluctuations. Comparing the case with $1/3\eta$ and the ideal case we still see larger fluctuations in the runs with $1/3\eta$, although the differences are not large.

3.2.3. Density vs velocity fluctuations

As explained in section 2.1, the density fluctuations are expected to scale linearly with velocity fluctuations. In the ICM, it has been found that the density fluctuations correlate with \mathcal{M}_{1D} with a slope close to 1 (Zhuravleva et al. 2014; Gaspari et al. 2014). However, this might also depend on the dynamical state of the cluster, where unrelaxed clusters might deviate from that value (Simonte et al. 2022; Zhuravleva et al. 2023). We want to investigate how viscosity affects that relation. To do so, we first calculate the velocity fluctuations via the root mean square velocity (v_{rms}) as

$$\delta v = \sqrt{(v_x - \langle v_x \rangle)^2 + (v_y - \langle v_y \rangle)^2 + (v_z - \langle v_z \rangle)^2}, \quad (18)$$

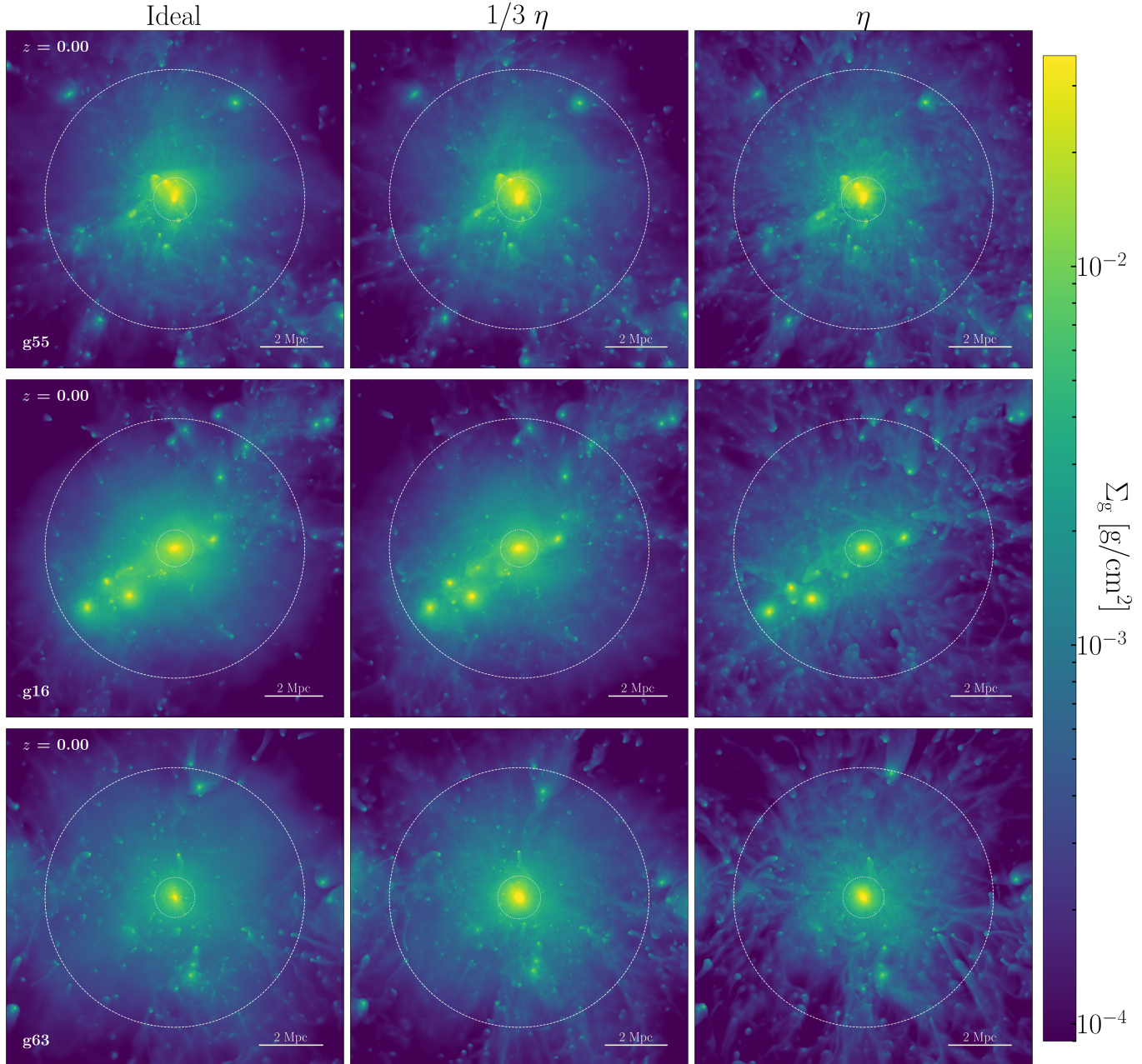


Figure 1. Density projections for all of our simulations listed in table 1. From left to right: MHD only, MHD with 1/3 of Spitzer viscosity and full Spitzer viscosity at redshift zero. From top to bottom: the runs g55, g16 and g63.

where $\langle v_x \rangle$, $\langle v_y \rangle$ and $\langle v_z \rangle$ are the mean velocities in each shell. We then calculate the 1D mach number of each particle as $\mathcal{M}_{1D} = \delta v / (c_s \sqrt{3})$. We take the region within R_{200c} of the cluster, similar to the one taken in Zhuravleva et al. (2023). For better statistics, we take the last 40 snapshots from $z \sim 0.4$ to $z = 0$ and calculate the mean value of density and velocity fluctuations of each shell in each snapshot using equations 17 and 18 respectively. For each snapshot we take the same radial bins normalised to R_{200c} . Finally, we take the mean value of the density and velocity fluctuations for each

shell over the snapshots and plot \mathcal{M}_{1D} against $\delta\rho/\rho$, as shown in Fig. 5. Since we have taken the average over a period of time, we cannot take into account the dynamical state of the clusters here.

There is a clear linear trend in all clusters, independently of the amount of viscosity, with a low scatter in all cases (the Pearson’s correlation coefficient is close to 1, indicating a good correlation). Viscosity reduces

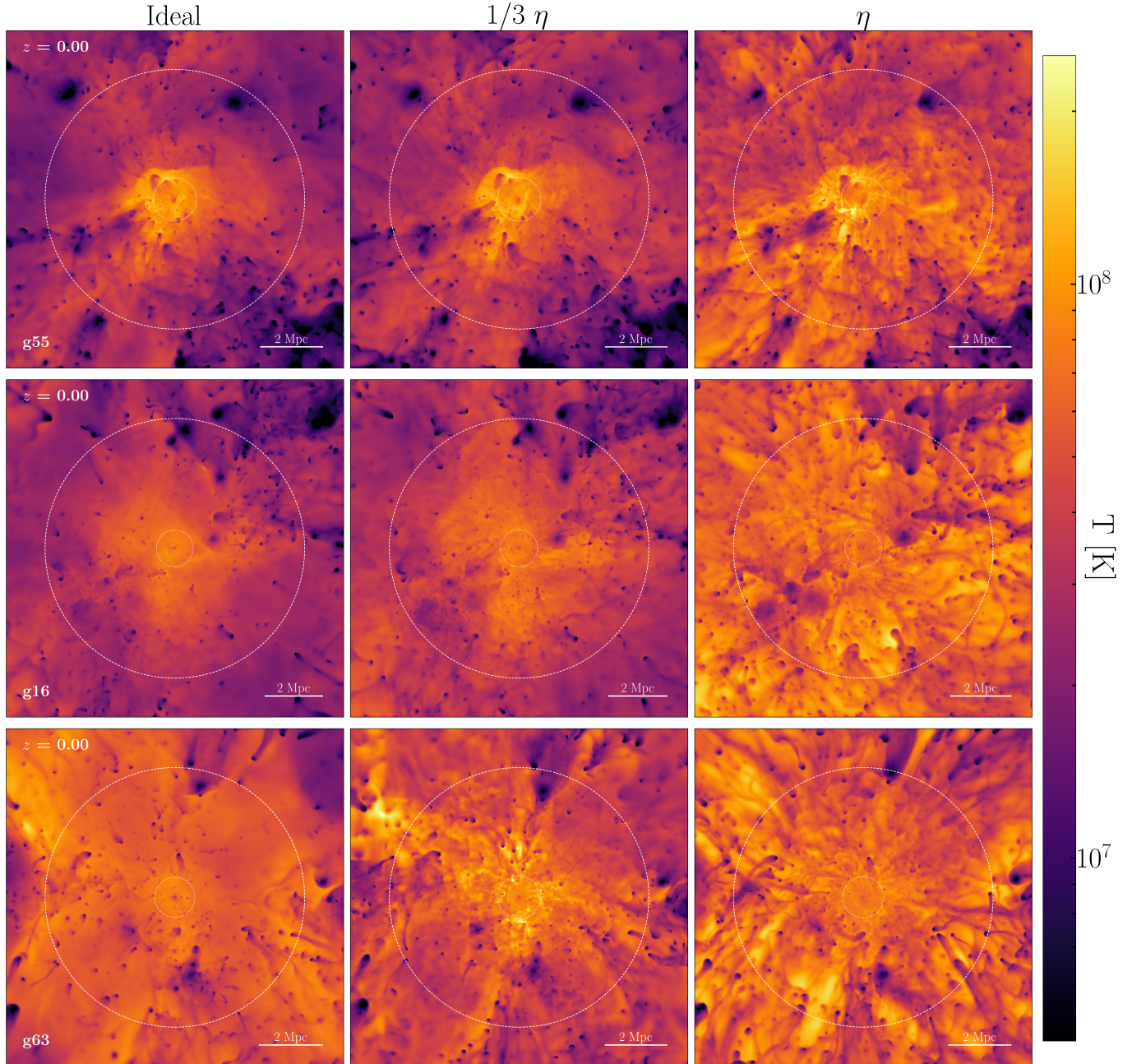


Figure 2. Temperature projections for all of our simulations listed in table 1. From left to right: MHD only, MHD with 1/3 of Spitzer viscosity and full Spitzer viscosity at redshift zero. From top to bottom: the runs g55, g16 and g63.

the slopes of the linear fits⁴. We observe that density and velocity fluctuations increase further from the center (lighter data points). This reflects the state of the ICM in clusters that keep growing by accretion (Zhuravleva et al. 2023). The values of \mathcal{M}_{1D} are consistent with direct observations of Perseus (Aharonian et al. 2018), where they found $\mathcal{M}_{3D} = \sqrt{3}\mathcal{M}_{1D} \simeq 0.3 - 0.45$ within

the central 100kpc of the cluster ($\sim 0.03R_{200c}$) and indirect measurements from observations (Lovisari et al. 2024; Dupourqué et al. 2024), with $\mathcal{M}_{3D} \simeq 0.36 - 0.41$ for relaxed clusters in the inner regions of the cluster (within $R_{500c} \sim 0.7R_{200c}$).

To study in more detail the ratio of density to velocity fluctuations, Fig. 6 shows the radial dependence of this ratio (η_ρ).

The cases with full viscosity have consistently a larger value of η_ρ , as a consequence of the shallower slope seen

⁴ Note that the slope is the inverse η_ρ .

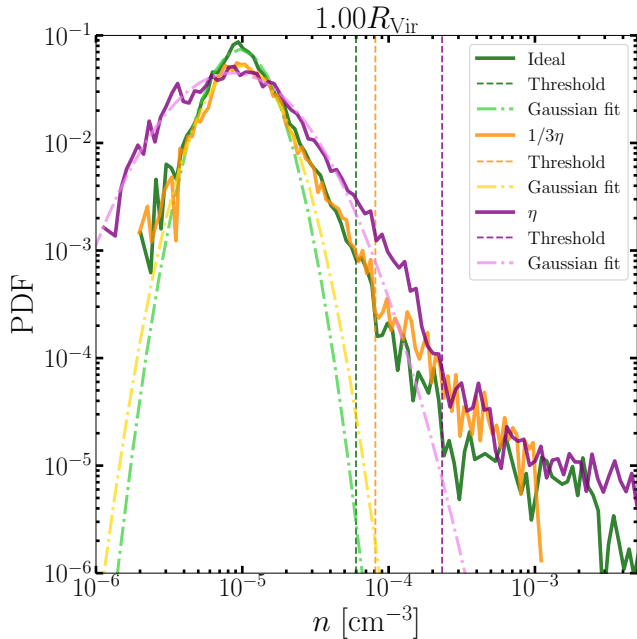


Figure 3. Density probability density function (PDF) of a thin shell of 5 kpc of the cluster g55 to show the effect of viscosity on the gas density distribution. The solid lines show the data; the vertical dashed lines indicate the values of the density thresholds separating bulk and high-density gas; and the dash-dotted lines the log-normal distribution fit to the bulk density component of the gas.

in Fig. 5. Cluster g63 shows a mean value closer to one (although a large scatter) in the inviscid case compared to clusters g55 and g16, all in agreement with the results found previously by Simonte et al. (2022) and Zhuravleva et al. (2023). The values of η_ρ in the cases with $1/3 \eta$ do not change significantly among the different clusters, whereas the runs with full viscosity have a larger value of η_ρ .

3.3. Comparison with observations

We have discussed the effects that viscosity has in galaxy clusters, focusing so far on the comparison between viscid and inviscid simulations. However, for a comparison with observations we need to calculate the 3D amplitude fluctuations as a function of the wavenumber $k = 1/l$ (where l is the length scale of the fluctuations). To do so, we first need to calculate the density fluctuations of our data elements and then compute the power spectrum. In particle based simulations the computation of the Fourier Transform to calculate the power spectrum is not possible, so we need to interpolate the particle properties onto a grid. By doing so, we also avoid spurious effects caused by the voids after removing the high-density regions (see section 3.2.1). In grid simulations, the voids are replaced by the median

value of the shell (e.g. Zhuravleva et al. 2023). In our case, the voids are automatically replaced by an average value over the particles of the region due to the interpolation method employed. This is done using the code VORTEX-P (Vallés-Pérez et al. 2021b,a, 2024), which creates an ad-hoc AMR mesh hierarchy from the density and velocity fields with the ultimate goal of providing a multi-resolution Helmholtz-Hodge and Reynolds decomposition. In this work, we use it exclusively to assign the density and velocity fields onto an AMR mesh, which is done using the same kernel configuration as for evolving the simulation. Once the particle data have been interpolated into the mesh, we calculate the density fluctuations. This is done by decomposing the density field into unperturbed and fluctuating components (Churazov et al. 2012):

$$\rho(x, y, z) = \rho_0(x, y, z)[1 + \delta(x, y, z)], \quad (19)$$

where $\rho_0(x, y, z)$ is the unperturbed density distribution and

$$\delta(x, y, z) = \frac{\delta\rho}{\rho_0} = \frac{|\rho_i - \rho_0|}{\rho_0} = \frac{|\rho_i - \langle\rho\rangle|}{\langle\rho\rangle} \quad (20)$$

are the fluctuations. ρ_i is the density of each cell and $\langle\rho\rangle$ is the value of the density profile at that distance from the center (see density profiles in appendix B). In our case, we evaluate the density profile at a given radius to estimate the unperturbed $\rho_0(x, y, z)$. For the power spectrum we assume an isotropic fluctuation field that is a function of $k = \sqrt{k_x^2 + k_y^2 + k_z^2}$. The 3D amplitude fluctuations can be computed from the power spectrum as

$$\left(\frac{\delta\rho}{\rho}\right)_k = \sqrt{4\pi P(k)k^3}, \quad (21)$$

where $P(k)$ is the power spectrum.

These 3D amplitude density fluctuations can be observed from X-ray emission and can be used to constrain the amount of viscosity in the ICM (Zhuravleva et al. 2019). Fig. 7 shows a comparison of density fluctuations of our sample of clusters for both unrelaxed (g55 and g16) and relaxed clusters (g63), with observations taken from Heinrich et al. (2024). The observational data is composed by 80 clusters (24 relaxed, 30 intermediate and 26 unrelaxed) of $M_{2500c} \in [8 \times 10^{13}, 10^{15}] M_\odot$, comparable to our sample (our clusters have $M_{2500c} \sim 2.4 - 3.9 \times 10^{14} M_\odot$). For a better comparison with observations, we take the same region of the cluster as in Heinrich et al. (2024), i.e. the gas inside R_{2500c} . The grey region indicates the average at each scale of the density fluctuations for the relaxed (unrelaxed) subsample plus/minus one standard deviation.

In all cases, viscosity leads to a larger amplitude of the fluctuations at all scales, leading to around two times

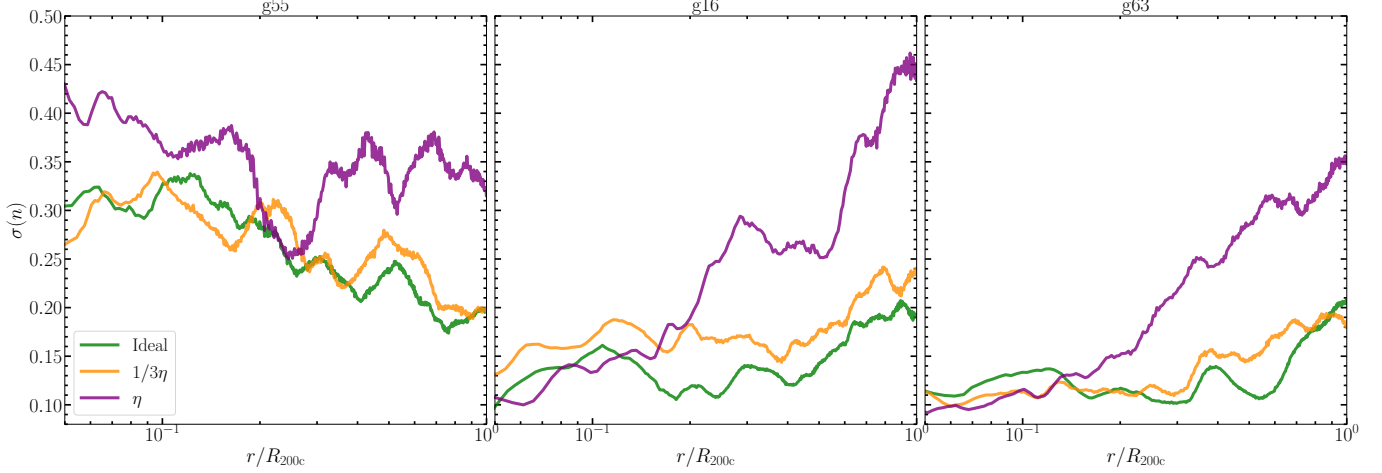


Figure 4. Radial profile of the standard deviation of the log-normal fit for each one of the spherical shells. From left to right: clusters g55, g16 and g63 for the different runs.

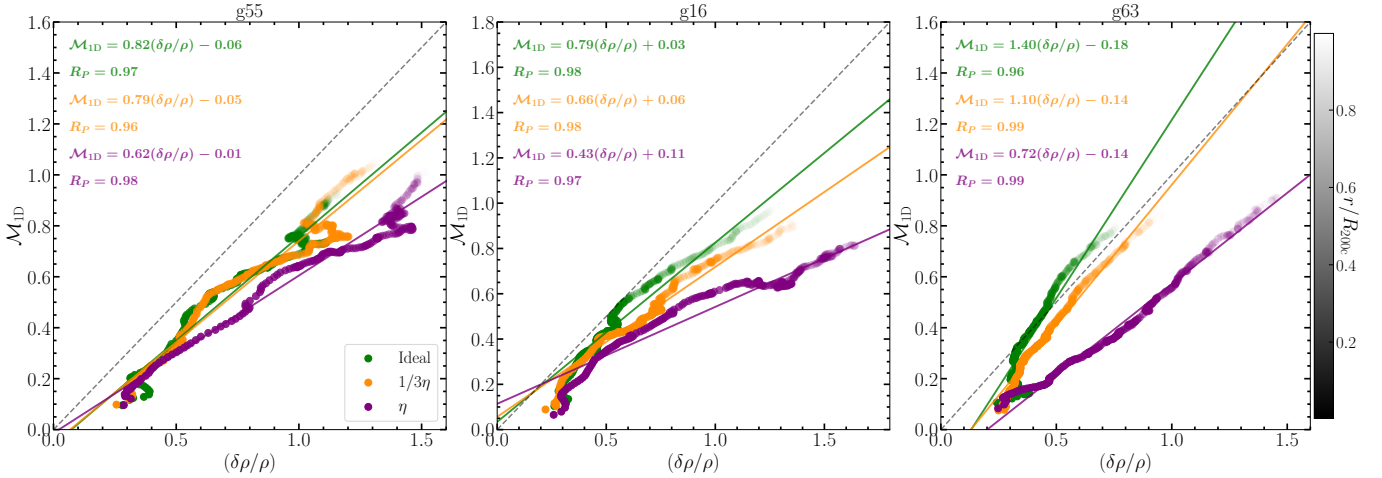


Figure 5. Velocity fluctuations against density fluctuations within R_{200c} . The transparency of the dots indicates the distance to the center of the cluster. The dots are calculated by averaging over 40 snapshots from redshift 0.4 to redshift 0 for each radial shell. For each of the runs we do a linear fit, indicating the slope, intercept and the Pearson's coefficient for each case. From left to right: clusters g55, g16 and g63 for each one of the configurations.

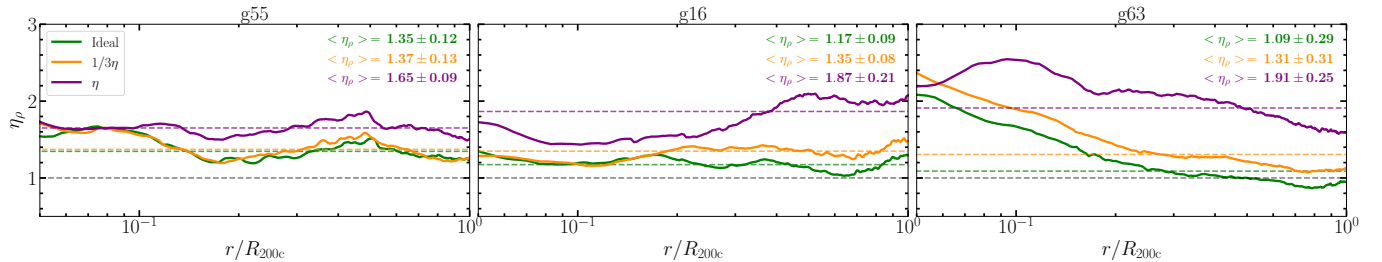


Figure 6. Ratio between density fluctuations and velocity fluctuations as a function of the radius within R_{200c} (same data as in Fig. 5). The solid lines indicate the data from the simulations, while the dashed lines indicate the mean value in each case within R_{200c} . The mean value and the standard deviation calculated over all the shells in each run is indicated in each panel. From left to right: clusters g55, g16 and g63 for each one of the configurations.

larger amplitude in the cases with full viscosity. Furthermore, the case with $1/3\eta$ has similar results compared to the non-viscous case in g55 and g63, but it is $\sim 30\%$ higher in g16. Although in cluster g55 the $1/3\eta$ and non-viscous runs are more consistent with observations, in clusters g16 and g63 the full viscosity case matches better the overall amplitude of observations. However, due to the small sample of simulations that we have, it is difficult to exclude any particular amount of viscosity by comparing our results with the overall amplitude of the observations.

To constrain the amount of viscosity in the ICM, Zhuravleva et al. (2019) suggested a criterion based on studying the slope of density fluctuations spectrum. In the cases with higher viscosity the turbulent cascade is stopped earlier, leading to a steeper power spectrum that translates into steeper 3D density amplitude fluctuations. This was probed by comparing Coma observations with direct numerical simulations (DNS) of hydrodynamic turbulence. They found a level of suppression of at least a factor of 10 with respect to the Spitzer value, depending on the Prandtl number⁵.

Assuming that the motions are subsonic and driven at large scales, one can assume that the fluctuations in the ICM are passively advected by the velocity field (Kunz et al. 2022). Therefore, a comparison with hydrodynamic turbulence simulation is somewhat reasonable. However, the DNS simulations employed in Zhuravleva et al. (2019) use a rather idealised setup, where compressible fluids (important mainly for unrelaxed clusters) or magnetic fields are not considered. They also assumed an isothermal fluid of $T_e \sim 8$ keV ($\sim 9.28 \times 10^7$ K) for Coma. And, since viscosity is highly dependent on the temperature (see equation 9), that means that they used a constant value of viscosity. This might produce the sharp viscous cutoff observed in their results. However, in cosmological simulations, we observe a range of temperatures from 3.3×10^6 K to 2.5×10^8 K, and therefore, a big range of values for viscosity. This range of values for viscosity at different scales prevents the power spectrum from having a sharp cutoff, as observed in Fig. 7 for density and Fig. 15 for velocities power spectrum. As a consequence, the slope of the 3D amplitude of density fluctuations is insensitive to the amount of viscosity. This is investigated in more detail in section 3.4.

It is important to note the maximum observed at $k \sim 2.5R_{2500c}^{-1} \sim 175$ kpc in the viscous runs of clus-

ters g16 and g63 in Fig. 7. This feature is not found either in observations or the other simulations, where the amplitude of density fluctuations decreases monotonically with k . The reason is the value of f_{cut} used in equation 14, where we used a value of $f_{\text{cut}} = 2.5$, the minimum value suggested in Zhuravleva et al. (2012). This value was reasonable for our cluster g55, where we have a clear separation of bulk gas following a log-normal distribution and a high-density tail (see Fig. 3). However, there is no clear separation between the bulk gas and high-density regions in the density PDF of cluster g16 (see appendix A) and g63, which looks more like a log-normal plus power law distribution. Due to its broad PDF, the median value is large and a value of $f_{\text{cut}} = 2.5$ sets a threshold at a large density value, causing very few or no particles to be considered as high-density (see Fig. 11). The small fraction of particles removed due to the choice of f_{cut} increases the amplitude density fluctuations at the scale of the high-density clumps (50 kpc - 200 kpc). A more reasonable value for this cluster would be $f_{\text{cut}} = 0.5$, where the split between bulk and high-density gas is more appropriate, as shown in the top panel of Fig. 12. With a lower value of f_{cut} , the maximum observed in the middle panel of Fig. 7 disappears, as can be seen in Fig. 13. However, the same value should be applied to all the analysis for consistency, and that would imply that in cluster g55 a lot of bulk gas would be considered as high-density gas (see bottom panel of Fig. 12). For this reason, we perform our analysis with a value of $f_{\text{cut}} = 2.5$, acknowledging that it has an impact on the viscous runs of clusters g16 and g63, leading to a factor of ~ 2 larger amplitude at the scales of the high-density clumps (~ 175 kpc). However, the slope of the density fluctuations is not affected by the choice of f_{cut} (see Fig. 13), indicating that the method to constrain viscosity is still robust regardless of the value of f_{cut} .

The code VORTEX-P also allows us to interpolate the velocity fluctuation field calculated from v_{rms} as shown in equation 18 and the soundspeed of each particle. Then we calculate the power spectrum of the velocity fluctuations in an analogous way as shown in equation 21

$$\left(\frac{\delta v}{c_s}\right)_k = \sqrt{4\pi P_{3D}(k)k^3} = \mathcal{M}_{3D,k}, \quad (22)$$

where $P_{3D}(k) = P_x(k) + P_y(k) + P_z(k)$. To obtain the 1D velocity fluctuations we do $\mathcal{M}_{1D,k} = \mathcal{M}_{3D,k}/\sqrt{3}$. Fig. 8 shows the velocity fluctuations for the three different clusters.

Since viscosity reduces the velocity of the particles (Marin-Gilabert et al. 2022) and, at the same time, increases the temperature (see section 3.1) and, therefore,

⁵ The Prandtl number is defined as the ratio of momentum to thermal diffusivity (i.e. the ratio between viscosity and thermal conduction).

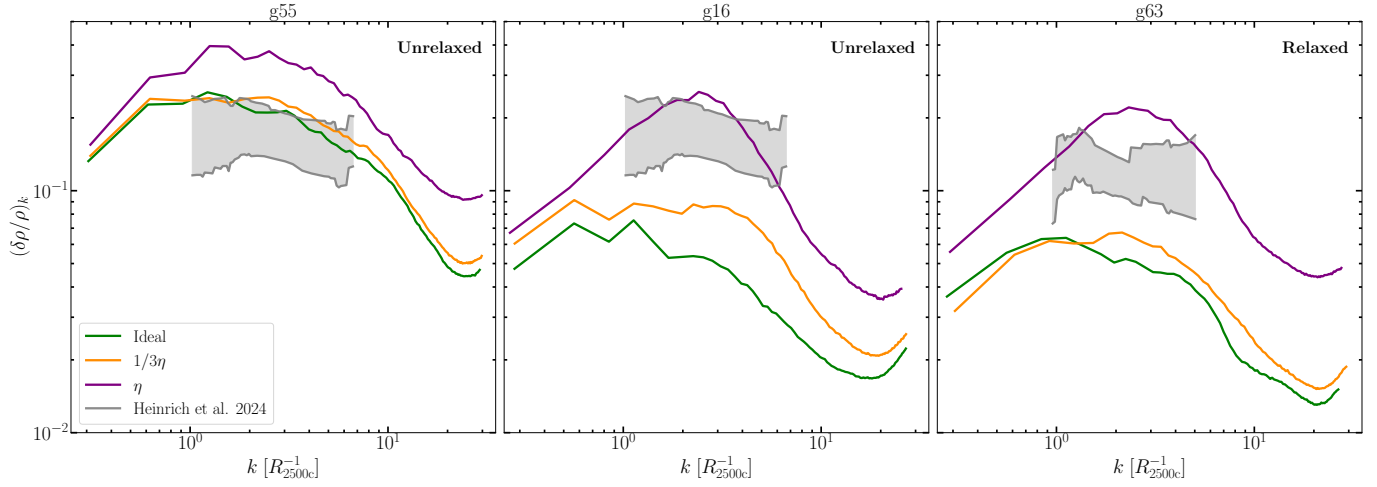


Figure 7. Comparison between density fluctuations obtained from our simulations with different viscosities (solid lines) and observations from Heinrich et al. (2024) (grey areas) as a function of the scale within R_{2500c} . From left to right: clusters g55, g16 and g63 for each one of the configurations. The unrelaxed clusters (g55 and g16) are compared with the observational data of unrelaxed clusters and the relaxed cluster (g63) with the observational data of relaxed clusters.

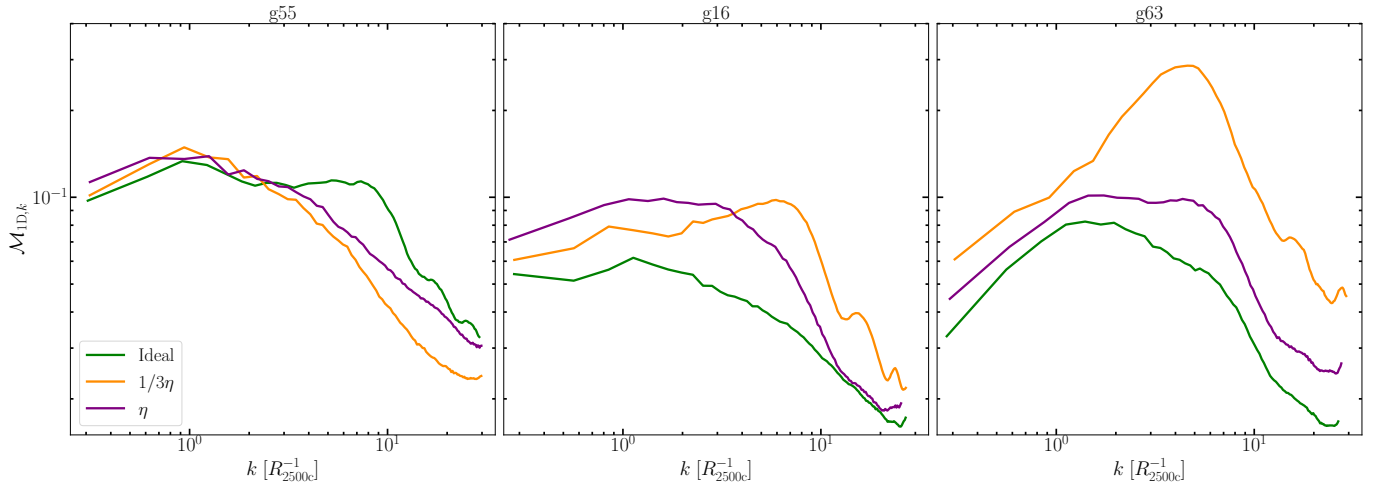


Figure 8. Comparison of velocity fluctuations obtained from our simulations with different viscosities as function of the scale within R_{2500c} . From left to right: clusters g55, g16 and g63 for each one of the configurations.

the soundspeed, one could expect that the $\mathcal{M}_{1D,k}$ decreases with viscosity. However, Fig. 8 shows very similar results among the simulations or even larger amplitude fluctuations in the viscous cases. This apparently counter-intuitive result might be due to the lack of mixing in the viscosity runs. This causes that the most massive structures in the cluster keep their mass for a longer time compared to the non-viscous runs, experiencing a larger gravitational pull and accelerating as they fall into the gravitational well of the cluster before being stripped. This can be observed also in the kinetic energy spectrum in appendix C, where at large scales the runs with viscosity lead to larger values of the energy spectrum.

Considering density and velocity fluctuations, we can study the relationship between the density and velocity fluctuations of equation 10. In Fig. 9 we show the value of $\eta_{\rho,k}$ calculated as $\eta_{\rho,k} = (\delta\rho/\rho)_k / \mathcal{M}_{1D,k}$ for different scales. The runs with greater viscosity tend to have larger values of $\eta_{\rho,k}$. This means that, even though both density and velocity fluctuations are higher in the viscous runs, they do not compensate for each other and the ratio between the two is still larger than for the non-viscous runs. The cluster g55 has values larger than 1, however this is in agreement with previous work for unrelaxed clusters (Gaspari et al. 2014; Simonte et al. 2022). The cluster g16 shows a relation very close to 1, as expected theoretically (Zhuravleva et al. 2014, 2023), although in the case with full viscosity we still see the

maximum analysed in appendix A. In cluster g63 we observe a value close to, but lower than 1, also consistent with previous work for a very relaxed cluster.

3.4. Thermodynamical structure

For a better understanding of the gas dynamics of the clusters, in this section, we study the thermodynamical structure of the different clusters. For a better comparison with observations, we focus only on the inner regions of the cluster (within R_{2500c}), as we did in previous sections. To visualize the thermodynamical structure of the clusters, Fig. 10 shows 2D histograms of the line-of-sight velocity (v_{LoS}) as a function of the temperature, color-coded by the emissivity. For the calculation of the emissivity, we assume it to be $\propto \rho^2 \sqrt{T}$, expected for thermal bremsstrahlung (Sarazin 1986). We also overplot the mass distribution of the particles as a contour for the different v_{LoS} and temperatures.

The unrelaxed dynamical state of cluster g55 (top row) can be identified by analysing the v_{LoS} , where the mass is distributed over a larger range of velocities. The emissivity is also distributed over a larger range of velocities and there is not a clear emissivity peak, as can be seen in the other two clusters. Although cluster g16 is unrelaxed and g63 is relaxed, the distributions of v_{LoS} look very similar, being approximately $v_{\text{LoS}} \in [-1000, 1000]$ km/s in both cases. The peak of emissivity in both g16 and g63 is localised around $v_{\text{LoS}} = 0$ km/s for all the configurations in the two clusters.

In all cases, the peak of emissivity is approximately between 10^7 and 10^8 K, within the range expected for galaxy clusters (Biffi et al. 2012). However, cluster g55 exhibits a broader temperature distribution due to its unrelaxed state, reaching temperatures of 5×10^8 K. The cases with full viscosity tend to have more mass at larger temperatures, as can be seen also in Fig. 2.

It is important to note that cluster g16 exhibits a narrower mass-weighted temperature distribution in the three configurations. The majority of the mass is concentrated in a narrow range of temperatures, meaning that this cluster is closer to being isothermal for the three runs than the other two clusters. This is similar to the case analysed by Zhuravleva et al. (2019), where they assumed an isothermal fluid of $T \sim 9.28 \times 10^7$ K for Coma. The narrower the temperature distribution is, the narrower is the range of viscosities as well (see equation 9). This would imply a sharper cutoff in the turbulent cascade, leading to a steeper 3D amplitude density fluctuations. Although cluster g16 is not perfectly isothermal, these steeper 3D amplitude density fluctuations can be seen in the middle panel of Fig. 7 by

comparing the non-viscous and the viscous case. The maximum produced by the choice of f_{cut} might affect the results, however the steeper spectrum can also be seen in Fig. 13 for different values of f_{cut} . The difference in slope is not as prominent as the one suggested by Zhuravleva et al. (2019), however, it indicates that their criterion to constrain viscosity might be applicable only to isothermal galaxy clusters. The consequence of the narrower temperature distribution can also be seen in the middle panel of Fig. 15, where the dynamical range of the spectrum reaches smaller scales in the non-viscous than in the viscous case.

Fig. 10 shows how a more isothermal cluster produces a steeper slope in the density fluctuations amplitude for the cases with viscosity compared to the inviscid cases. However, the differences in the slope vanish if the temperature distribution within the cluster is broader.

4. CONCLUSIONS

In this work we performed a set of cosmological simulations using the code OPENGADGET3 of three different galaxy clusters, each with three different values of viscosity to quantify the effect of viscosity in the ICM. First, we compared the results of these simulations at redshift zero in order to understand the effect that viscosity has in the ICM. Then we tried to constrain the amount of viscosity in the ICM by comparing with X-ray observations of density fluctuations. Our key conclusions are:

- Although the overall morphology remains the same, by visual inspection one can identify morphological differences produced by viscosity due the suppression of instabilities on small scales. The runs with more viscosity show a larger amount of small clumps that have not been disrupted by instabilities; a more filamentary structure produced by the gas stripped from infalling structures towards the center of the cluster; and more gas concentrated in the denser regions, rather than the more mixed and homogeneous gas seen in the non-viscous cases.
- The kinetic energy transformed into internal energy by viscosity leads to the heating of the less dense regions, although the denser regions remain as cold as in the inviscid runs. This is translated into a higher virial temperature in the runs with viscosity by $\sim 5\%$ - 10% .
- The lack of mixing in the viscous case produces a broader density PDF of the bulk gas of the cluster, which can be interpreted as larger density fluctuations. The density fluctuations are consistently larger along the cluster radius the more viscous

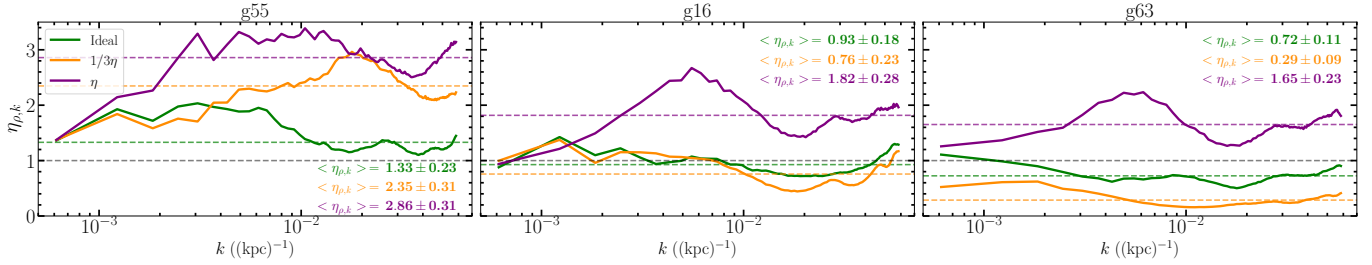


Figure 9. Ratio between density fluctuations and velocity fluctuations as function of the scale within R_{2500c} . The solid lines indicate the data from the simulations, while the dashed lines indicate the mean value in each case along the different scales. The mean value and the standard deviation in each run is indicated in each panel. From left to right: clusters g55, g16 and g63 for each one of the configurations.

the medium is, increasing towards longer distances from the center.

- Using a fixed value of f_{cut} , used to divide the bulk and high-density gas, works well for inviscid simulations of galaxy clusters. However, the results with full viscosity (where the density PDF is broader) are slightly dependent on the choice of f_{cut} . Therefore, a more accurate method to separate bulk and high-density gas should be investigated in the future to avoid the dependence on the shape of the density PDF.
- The density and velocity fluctuations are directly proportional to one another and both increase with the distance from the center. However, in all three clusters the slope of the relationship between velocity and density fluctuations decreases with increasing viscosity. This linear relation is translated into a density to velocity fluctuations ratio of the order of unity for distances up to R_{200c} .
- The runs with viscosity tend to have larger amplitude of density fluctuations as a function of the scale. However, the density fluctuations obtained from our simulations are consistent with observations, even in the case with full viscosity. This is due to the large range of temperature distribution. In isothermal clusters, the slope of the amplitude of density fluctuations is affected by viscosity. This means that the method suggested in Zhuravleva et al. (2019) to constrain the amount of viscosity in the ICM by measuring the slope of the amplitude of density fluctuations is only applicable to isothermal clusters.
- The amplitude of velocity fluctuations also appears to increase with viscosity, mainly at large scales. This behaviour can also be observed when computing the velocity power spectrum, where viscosity leads to more power at large scales, but decreases at smaller scales. The ratio of density to

velocity fluctuations tends to be higher for cases with full viscosity, while remaining close to unity for all cases regardless of the amount of viscosity.

In summary, the cosmological simulations with viscosity show some morphological differences as well as temperature differences. We can quantify these morphological differences by measuring the fluctuations in density, which become larger in the cases with higher viscosity. This can be compared with observational measurements of the amplitude of density fluctuations. Our results are consistent with observations, making difficult the task of constraining the amount of viscosity in the ICM solely from density fluctuations. The velocity fluctuations also happen to be larger at large scales in the cases with viscosity, although the ratio of density to velocity fluctuations is larger with viscosity, but close to one.

Due to the computational costs of running cosmological simulations at high resolution including physical viscosity, we could only compare three different galaxy clusters. Future work with more clusters could help us in doing statistics and not relying our results in three clusters only. Higher resolution simulations could also help us to understand better the results and avoid spurious resolution effects. Additionally, the effect of a more realistic anisotropic Braginskii viscosity cosmological simulation will be explored in future studies.

DATA AVAILABILITY

The data will be made available based on reasonable request to the corresponding author.

ACKNOWLEDGMENTS

TM would like to thank Irina Zhuravleva and Eugene Churazov for the intense discussions which motivated this work. The authors also want to thank the referee for their very useful comments. KD and TM acknowledge support by the COMPLEX project from the European Research Council (ERC) under the European

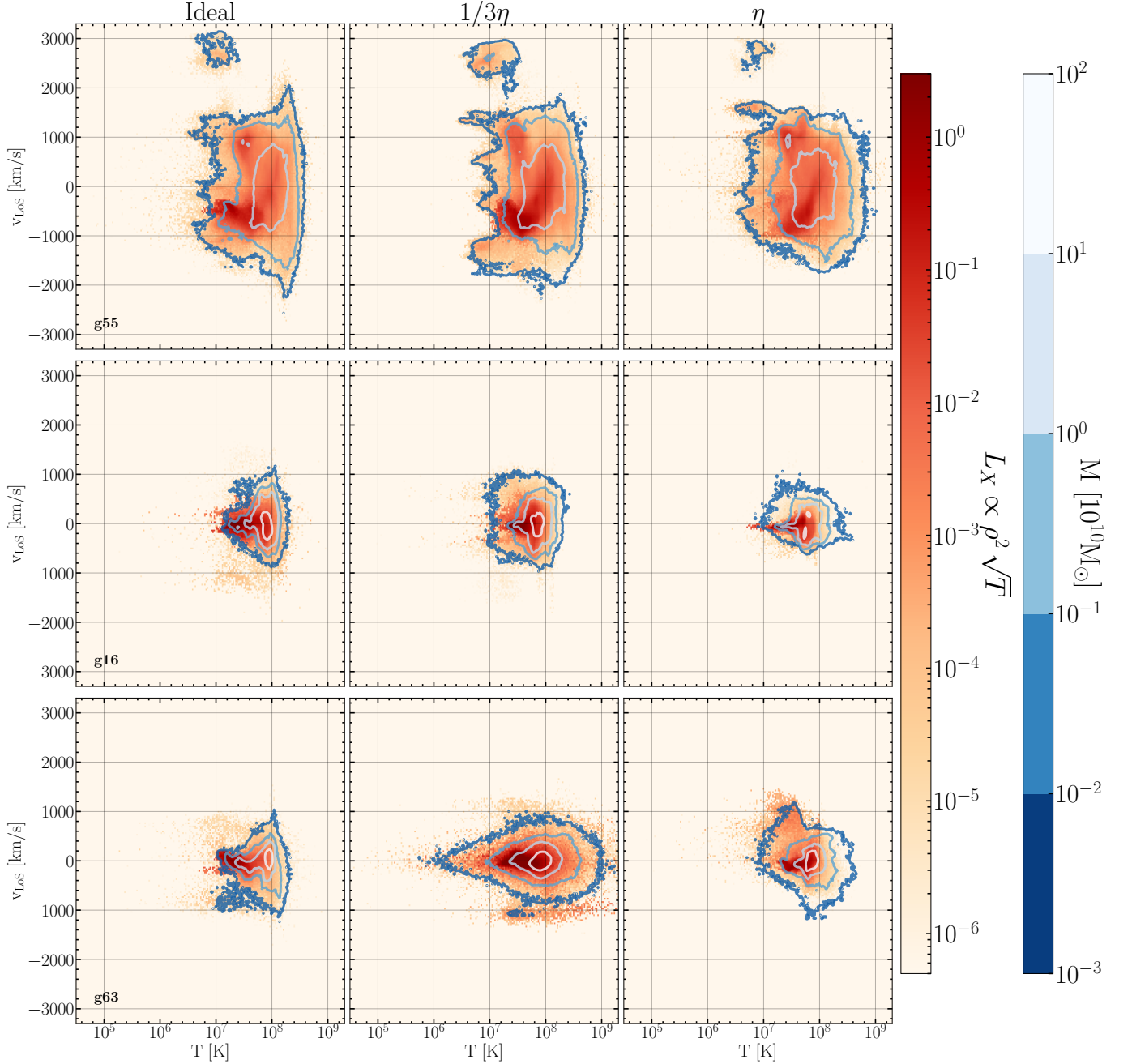


Figure 10. 2D histograms of the v_{LOS} as a function of the temperature, color-coded by emissivity. The contours indicate the mass distribution of the particles within the cluster. From left to right: MHD only, MHD with 1/3 of Spitzer viscosity and full Spitzer viscosity at redshift zero. From top to bottom: clusters g55, g16 and g63.

Union’s Horizon 2020 research and innovation program grant agreement ERC-2019-AdG 882679. UPS is supported by the Simons Foundation through a Flatiron Research Fellowship (FRF) a the Center for Computational Astrophysics (CCA). The CCA is supported by the Simons Foundation. MV is supported by the Italian Research Center on High Performance Computing, Big Data and Quantum Computing (ICSC), project funded by European Union - NextGenerationEU - and

National Recovery and Resilience Plan (NRRP) - Mission 4 Component 2, within the activities of Spoke 3, Astrophysics and Cosmos Observations, and by the INFN Indark Grant. DVP has been supported by the Agencia Estatal de Investigación Española (AEI; grant PID2022-138855NB-C33), by the Ministerio de Ciencia e Innovación (MCIN) within the Plan de Recuperación, Transformación y Resiliencia del Gobierno de España through the project ASFAE/2022/001, with funding from Eu-

ropean Union NextGenerationEU (PRTR-C17.I1), by the Generalitat Valenciana (grant CIPROM/2022/49), and by Universitat de València through an Atracció de Talent fellowship. This work has been supported by the Munich Excellence Cluster Origins funded by the

Deutsche Forschungsgemeinschaft (DFG, German Research Foundation) under Germany’s Excellence Strategy EXC-2094 390783311. The simulations were performed at the Computational Center for Particle and Astrophysics (C2PAP).

APPENDIX

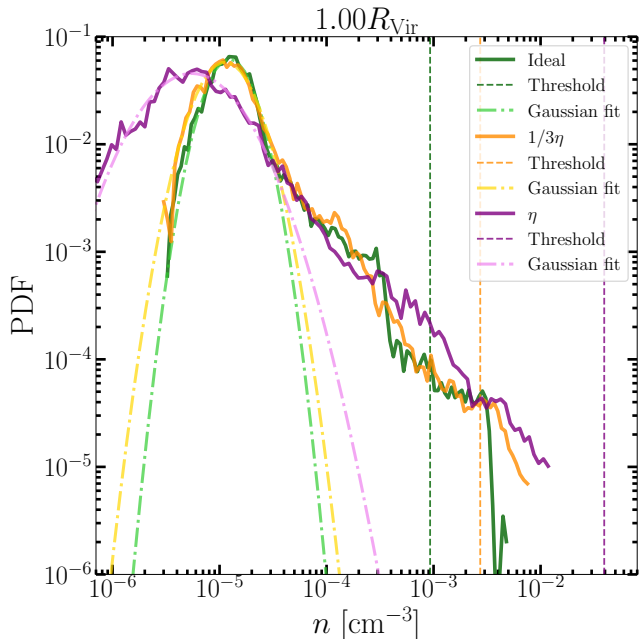


Figure 11. Density PDF of a 5kpc shell centered around the virial radius of cluster g16 using a value of $f_{\text{cut}} = 2.5$. The solid lines show the data obtained from the simulations; the dashed lines the calculated threshold to split bulk and high-density gas; and the dashed-dotted lines the fit of the bulk gas to a log-normal distribution.

A. DEPENDENCE ON f_{cut}

Viscosity broadens the density PDF due to the lack of mixing. As a result, it becomes difficult to define a dividing line between the bulk and the high-density gas. The median value of density is displaced towards larger values of density, causing the threshold defined in equation 14 to be a poor choice for the division between bulk and high-density gas. In the most extreme cases, this threshold lies outside the range of densities for certain shells of the cluster, as can be seen in Fig. 11 for cluster g16 for $f_{\text{cut}} = 2.5$.

This signifies that some high-density clumps are not removed, leading to the maximum in the density fluctuations spectrum, as shown in Fig. 7. This can be solved by reducing the value of f_{cut} in equation 14 to lower values than 2.5. By doing this, we can successfully split bulk and high-density gas, as can be seen in the upper

panel of Fig. 12, where we used $f_{\text{cut}} = 0.5$. As a consequence, the maximum observed in the amplitude of the density fluctuations is reduced (see Fig. 13). However, if we use $f_{\text{cut}} = 0.5$ in other clusters, the split of bulk and high-density gas is not properly done (see bottom panel of Fig. 12 to observe the effect in cluster g55). This value of f_{cut} would consider part of the bulk gas as high-density gas and would remove more gas than only high-density clumps. For consistency we use the same value of f_{cut} in all our clusters, choosing the value suggested in Zhuravleva et al. (2012) of $f_{\text{cut}} = 2.5$ and acknowledging the spurious effects that it can have in the amplitude of density fluctuations.

B. DENSITY PROFILE

If we look at the radial density profile of each one of the clusters (Fig. 14) we do not observe any clear trend among the cases with different viscosities. This shows how at large scales the viscosity effects do not significantly affect the cluster morphology. We need to study the density fluctuations ($\sim 5\%$ - 10% of the total density (Churazov et al. 2012; Sanders & Fabian 2012)) to see bigger differences between the cases with and without viscosity. When making a radial profile, using the mean density for each shell hides the main impact of the viscosity, which is seen in the fluctuations about the mean. Fig. 3 shows how, even though the density distribution is broader with viscosity, the mean value remains more or less the same, leading to very similar radial density profiles.

C. VELOCITY POWER SPECTRUM

We can make use of the code VORTEX-P to interpolate the particles into a grid and compute the velocity power spectrum for each cluster and for each amount of viscosity in each case. Fig. 15 shows the power spectrum normalised to Kolmogorov for each cluster within R_{2500c} . In all cases the slope is steeper than Kolmogorov, however, the slope is the same in each cluster regardless the amount of viscosity. At larger scales the runs with viscosity appear to be more energetic, although at intermediate and small scales the viscosity runs become less energetic (except for the cluster g16).

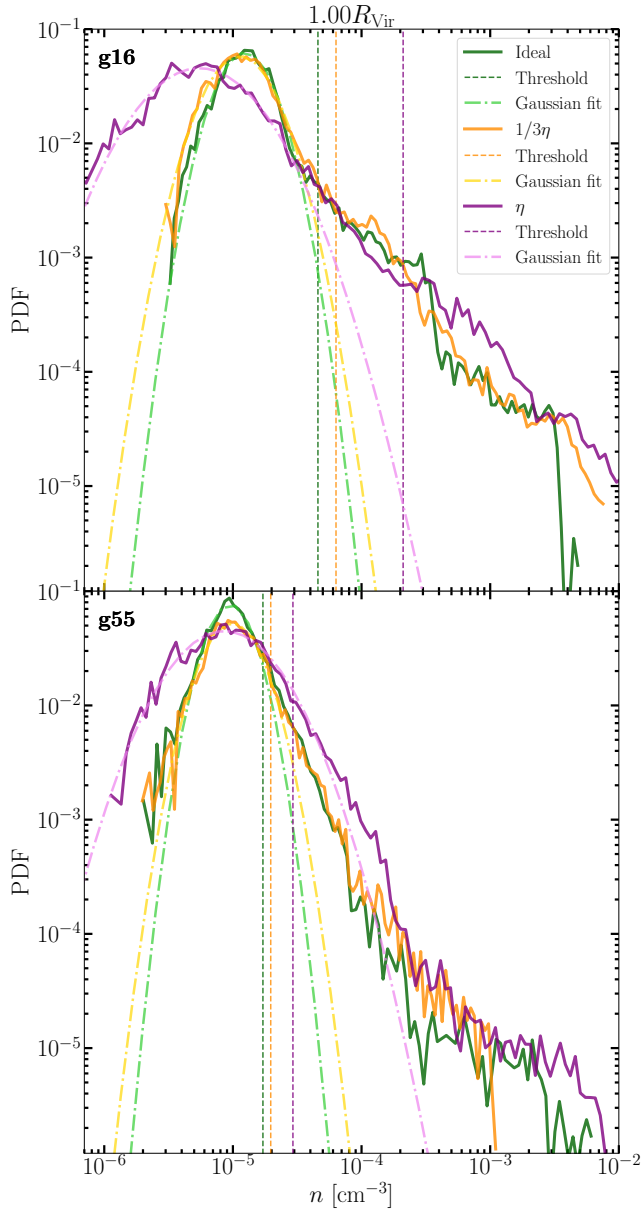


Figure 12. Density PDF of a 5kpc shell centered around the virial radius using a value of $f_{\text{cut}} = 0.5$. The solid lines show the data obtained from the simulations; the dashed lines the calculated threshold to split bulk and high-density gas; and the dashed-dotted line the fit of the bulk gas to a log-normal distribution. *Top panel:* cluster g16. *Bottom panel:* cluster g55.

REFERENCES

- Aharonian, F., Akamatsu, H., Akimoto, F., et al. 2018, Publications of the Astronomical Society of Japan, 70, doi: [10.1093/pasj/psx138](https://doi.org/10.1093/pasj/psx138)
- Arth, A., Dolag, K., Beck, A. M., Petkova, M., & Lesch, H. 2017, Anisotropic thermal conduction in galaxy clusters with MHD in Gadget. <https://arxiv.org/abs/1412.6533>
- Balsara, D. S. 1995, Journal of Computational Physics, 121, 357, doi: [https://doi.org/10.1016/S0021-9991\(95\)90221-X](https://doi.org/10.1016/S0021-9991(95)90221-X)
- Beck, A. M., Murante, G., Arth, A., et al. 2016, MNRAS, 455, 2110, doi: [10.1093/mnras/stv2443](https://doi.org/10.1093/mnras/stv2443)

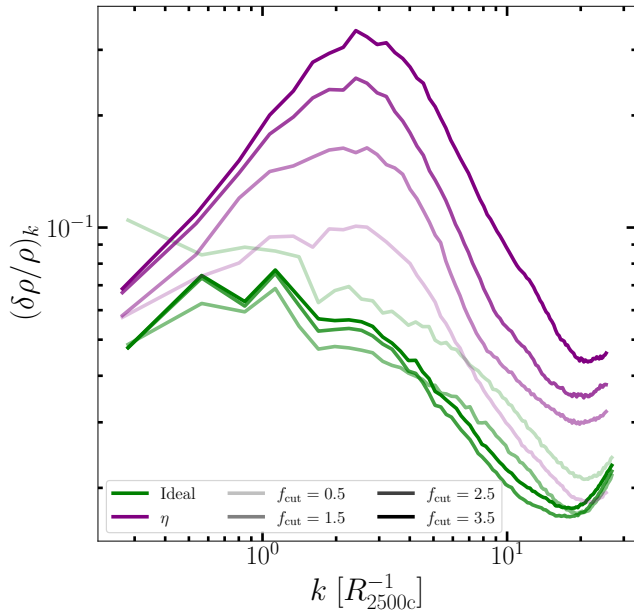


Figure 13. Comparison of the amplitude of density fluctuations in cluster g16 for different values of f_{cut} with and without viscosity.

- Berlok, T., Pakmor, R., & Pfrommer, C. 2019, Monthly Notices of the Royal Astronomical Society, 491, 2919–2938, doi: [10.1093/mnras/stz3115](https://doi.org/10.1093/mnras/stz3115)
- Berlok, T., Quataert, E., Pessah, M. E., & Pfrommer, C. 2021, MNRAS, 504, 3435, doi: [10.1093/mnras/stab832](https://doi.org/10.1093/mnras/stab832)
- Biffi, V., Dolag, K., & Böhringer, H. 2012, Monthly Notices of the Royal Astronomical Society, 428, 1395–1409, doi: [10.1093/mnras/sts120](https://doi.org/10.1093/mnras/sts120)
- Bonafede, A., Dolag, K., Stasyszyn, F., Murante, G., & Borgani, S. 2011, Monthly Notices of the Royal Astronomical Society, 418, 2234–2250, doi: [10.1111/j.1365-2966.2011.19523.x](https://doi.org/10.1111/j.1365-2966.2011.19523.x)
- Braginskii, S. I. 1965, Reviews of Plasma Physics, 1, 205
- Brunetti, G., & Lazarian, A. 2007, Monthly Notices of the Royal Astronomical Society, 378, 245, doi: [10.1111/j.1365-2966.2007.11771.x](https://doi.org/10.1111/j.1365-2966.2007.11771.x)
- Brüggen, M., van Weeren, R. J., & Röttgering, H. J. A. 2012, Monthly Notices of the Royal Astronomical Society: Letters, 425, L76–L80, doi: [10.1111/j.1745-3933.2012.01304.x](https://doi.org/10.1111/j.1745-3933.2012.01304.x)
- Churazov, E., Forman, W., Jones, C., Sunyaev, R., & Böhringer, H. 2004, Monthly Notices of the Royal Astronomical Society, 347, 29, doi: [10.1111/j.1365-2966.2004.07201.x](https://doi.org/10.1111/j.1365-2966.2004.07201.x)
- Churazov, E., Vikhlinin, A., Zhuravleva, I., et al. 2012, Monthly Notices of the Royal Astronomical Society, 421, 1123–1135, doi: [10.1111/j.1365-2966.2011.20372.x](https://doi.org/10.1111/j.1365-2966.2011.20372.x)
- Cowie, L. L., & McKee, C. F. 1977, ApJ, 211, 135, doi: [10.1086/154911](https://doi.org/10.1086/154911)
- Cui, W., Power, C., Borgani, S., et al. 2016, Monthly Notices of the Royal Astronomical Society, 464, 2502, doi: [10.1093/mnras/stw2567](https://doi.org/10.1093/mnras/stw2567)
- Cullen, L., & Dehnen, W. 2010, Monthly Notices of the Royal Astronomical Society, 408, 669–683, doi: [10.1111/j.1365-2966.2010.17158.x](https://doi.org/10.1111/j.1365-2966.2010.17158.x)
- Das, H. K., & Gronke, M. 2023, Monthly Notices of the Royal Astronomical Society, 527, 991, doi: [10.1093/mnras/stad3125](https://doi.org/10.1093/mnras/stad3125)
- Dehnen, W., & Aly, H. 2012, Monthly Notices of the Royal Astronomical Society, 425, 1068–1082, doi: [10.1111/j.1365-2966.2012.21439.x](https://doi.org/10.1111/j.1365-2966.2012.21439.x)
- Dolag, K., Vazza, F., Brunetti, G., & Tormen, G. 2005, Monthly Notices of the Royal Astronomical Society, 364, 753–772, doi: [10.1111/j.1365-2966.2005.09630.x](https://doi.org/10.1111/j.1365-2966.2005.09630.x)
- Dong, R., & Stone, J. M. 2009, The Astrophysical Journal, 704, 1309–1320, doi: [10.1088/0004-637x/704/2/1309](https://doi.org/10.1088/0004-637x/704/2/1309)
- Dupourqué, S., Clerc, N., Pointecouteau, E., et al. 2024, CHEX-MATE : turbulence in the ICM from X-ray surface brightness fluctuations. <https://arxiv.org/abs/2403.03064>
- Faltenbacher, A., Kravtsov, A. V., Nagai, D., & Gottlöber, S. 2005, Monthly Notices of the Royal Astronomical Society, 358, 139, doi: [10.1111/j.1365-2966.2005.08769.x](https://doi.org/10.1111/j.1365-2966.2005.08769.x)
- Federrath, C. 2016, Journal of Physics: Conference Series, 719, 012002, doi: [10.1088/1742-6596/719/1/012002](https://doi.org/10.1088/1742-6596/719/1/012002)
- Fujita, Y., Takizawa, M., & Sarazin, C. L. 2003, The Astrophysical Journal, 584, 190–202, doi: [10.1086/345599](https://doi.org/10.1086/345599)
- Gaspari, M. 2015, Monthly Notices of the Royal Astronomical Society: Letters, 451, L60–L64, doi: [10.1093/mnrasl/slv067](https://doi.org/10.1093/mnrasl/slv067)
- Gaspari, M., Churazov, E., Nagai, D., Lau, E. T., & Zhuravleva, I. 2014, A&A, 569, A67, doi: [10.1051/0004-6361/201424043](https://doi.org/10.1051/0004-6361/201424043)
- Gilfanov, M. R., Syunyaev, R. A., & Churazov, E. M. 1987, Soviet Astronomy Letters, 13, 3
- Gisler, G. R. 1976, A&A, 51, 137
- Groth, F., Steinwandel, U. P., Valentini, M., & Dolag, K. 2023, Monthly Notices of the Royal Astronomical Society, 526, 616, doi: [10.1093/mnras/stad2717](https://doi.org/10.1093/mnras/stad2717)
- Heinrich, A., Zhuravleva, I., Zhang, C., et al. 2024, Monthly Notices of the Royal Astronomical Society, 528, 7274, doi: [10.1093/mnras/stae208](https://doi.org/10.1093/mnras/stae208)
- Hu, C.-Y., Naab, T., Walch, S., Moster, B. P., & Oser, L. 2014, Monthly Notices of the Royal Astronomical Society, 443, 1173–1191, doi: [10.1093/mnras/stu1187](https://doi.org/10.1093/mnras/stu1187)

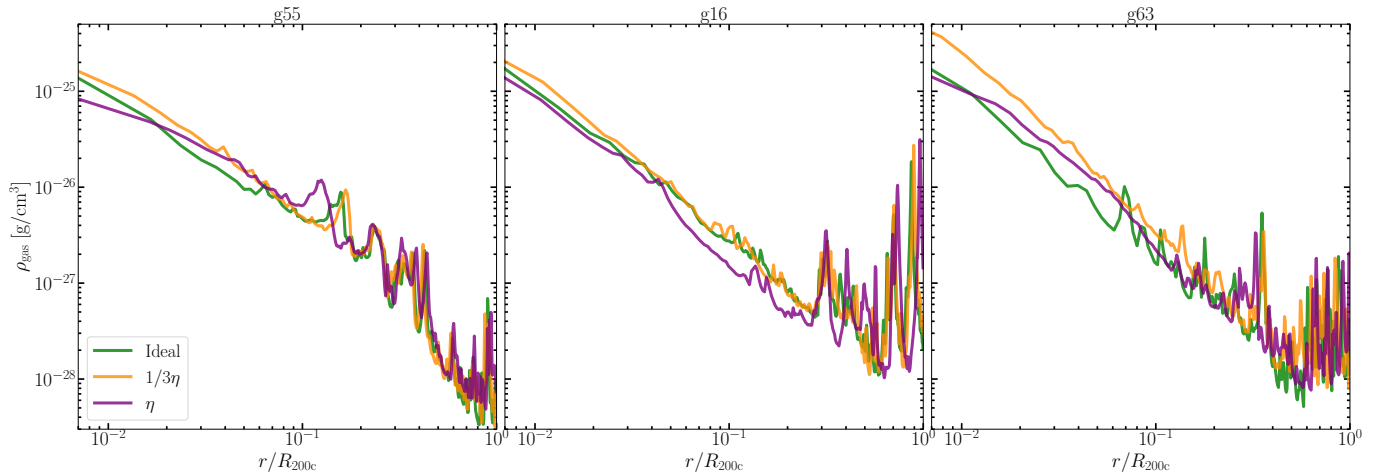


Figure 14. Radial profile of the density computed from spherical shells of 10kpc. From left to right: clusters g55, g16 and g63 for each one of the configurations.

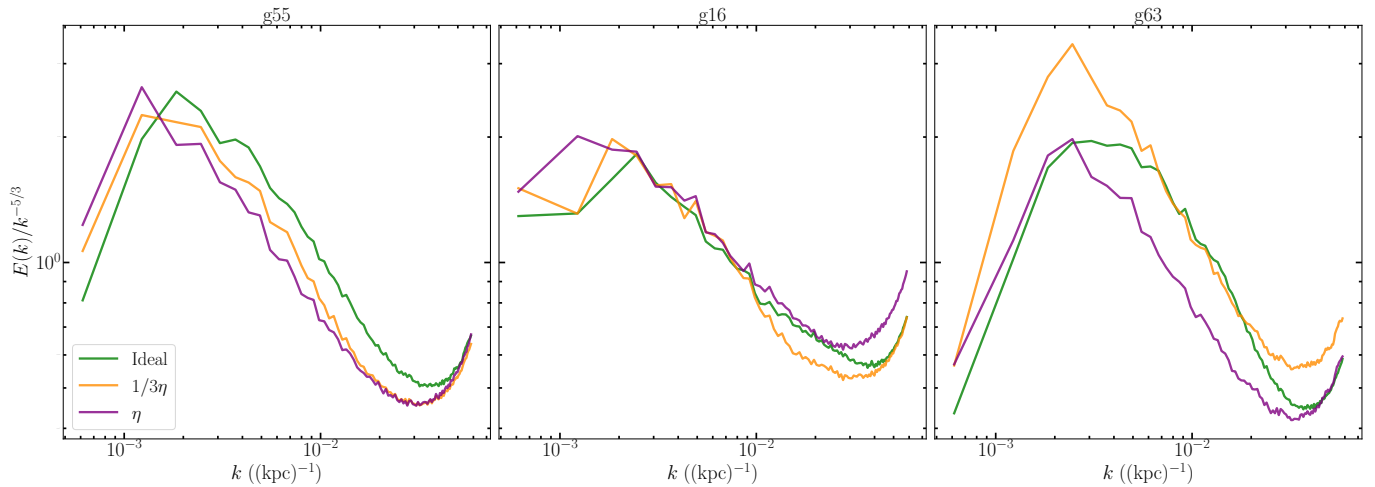


Figure 15. Velocity power spectrum normalised to Kolmogorov. From left to right: clusters g55, g16 and g63 for each one of the configurations.

Iapichino, L., Federrath, C., & Klessen, R. S. 2017, *Monthly Notices of the Royal Astronomical Society*, 469, 3641–3655, doi: [10.1093/mnras/stx882](https://doi.org/10.1093/mnras/stx882)

Kazantsev, A. P. 1968, *Soviet Journal of Experimental and Theoretical Physics*, 26, 1031

Klein, R. I., McKee, C. F., & Colella, P. 1994, *ApJ*, 420, 213, doi: [10.1086/173554](https://doi.org/10.1086/173554)

Kolmogorov, A. 1941, *Rep. AS USSR*, 30, 299

Kolmogorov, A. N. 1962, *Journal of Fluid Mechanics*, 13, 82–85, doi: [10.1017/S0022112062000518](https://doi.org/10.1017/S0022112062000518)

Kraft, R. P., Roediger, E., Machacek, M., et al. 2017, *The Astrophysical Journal*, 848, 27, doi: [10.3847/1538-4357/aa8a6e](https://doi.org/10.3847/1538-4357/aa8a6e)

Kravtsov, A. V., & Borgani, S. 2012, *ARA&A*, 50, 353, doi: [10.1146/annurev-astro-081811-125502](https://doi.org/10.1146/annurev-astro-081811-125502)

Kulsrud, R. M., & Anderson, S. W. 1992, *ApJ*, 396, 606, doi: [10.1086/171743](https://doi.org/10.1086/171743)

Kunz, M., Schekochihin, A., & Stone, J. 2014, *Physical Review Letters*, 112, doi: [10.1103/PhysRevLett.112.205003](https://doi.org/10.1103/PhysRevLett.112.205003)

Kunz, M. W., Jones, T. W., & Zhuravleva, I. 2022, *Plasma Physics of the Intracluster Medium* (Springer Nature Singapore), 1–42, doi: [10.1007/978-981-16-4544-0_125-1](https://doi.org/10.1007/978-981-16-4544-0_125-1)

Lovisari, L., Ettori, S., Rasia, E., et al. 2024, *A&A*, 682, A45, doi: [10.1051/0004-6361/202346651](https://doi.org/10.1051/0004-6361/202346651)

Marin-Gilabert, T., Valentini, M., Steinwandel, U. P., & Dolag, K. 2022, *Monthly Notices of the Royal Astronomical Society*, 517, 5971–5991, doi: [10.1093/mnras/stac3042](https://doi.org/10.1093/mnras/stac3042)

- Mohapatra, R., Federrath, C., & Sharma, P. 2020, *Monthly Notices of the Royal Astronomical Society*, 493, 5838–5853, doi: [10.1093/mnras/staa711](https://doi.org/10.1093/mnras/staa711)
- Monaghan, J., & Gingold, R. 1983, *Journal of Computational Physics*, 52, 374, doi: [https://doi.org/10.1016/0021-9991\(83\)90036-0](https://doi.org/10.1016/0021-9991(83)90036-0)
- Monaghan, J. J. 1992, *Annual Review of Astronomy and Astrophysics*, 30, 543, doi: [10.1146/annurev.aa.30.090192.002551](https://doi.org/10.1146/annurev.aa.30.090192.002551)
- Nulsen, P. E. J. 1982, *MNRAS*, 198, 1007, doi: [10.1093/mnras/198.4.1007](https://doi.org/10.1093/mnras/198.4.1007)
- O’Neill, S. M., Young, D. S. D., & Jones, T. W. 2009, *The Astrophysical Journal*, 694, 1317, doi: [10.1088/0004-637X/694/2/1317](https://doi.org/10.1088/0004-637X/694/2/1317)
- Pakmor, R., Springel, V., Coles, J. P., et al. 2023, *Monthly Notices of the Royal Astronomical Society*, 524, 2539–2555, doi: [10.1093/mnras/stac3620](https://doi.org/10.1093/mnras/stac3620)
- Pitaevskii, L. P., & Lifshitz, E. M. 1981, *Physical Kinetics: Volume 10 (Course of Theoretical Physics)*
- Pittard, J. M., Dyson, J. E., Falle, S. A. E. G., & Hartquist, T. W. 2005, *Monthly Notices of the Royal Astronomical Society*, 361, 1077–1090, doi: [10.1111/j.1365-2966.2005.09268.x](https://doi.org/10.1111/j.1365-2966.2005.09268.x)
- Power, C., Knebe, A., & Knollmann, S. R. 2012, *MNRAS*, 419, 1576, doi: [10.1111/j.1365-2966.2011.19820.x](https://doi.org/10.1111/j.1365-2966.2011.19820.x)
- Price, D. J. 2008, *Journal of Computational Physics*, 227, 10040, doi: <https://doi.org/10.1016/j.jcp.2008.08.011>
- . 2012, *Journal of Computational Physics*, 231, 759–794, doi: [10.1016/j.jcp.2010.12.011](https://doi.org/10.1016/j.jcp.2010.12.011)
- Ragone-Figueroa, C., Granato, G. L., Murante, G., Borgani, S., & Cui, W. 2013, *Monthly Notices of the Royal Astronomical Society*, 436, 1750–1764, doi: [10.1093/mnras/stt1693](https://doi.org/10.1093/mnras/stt1693)
- Randall, S., Nulsen, P., Forman, W. R., et al. 2008, *The Astrophysical Journal*, 688, 208–223, doi: [10.1086/592324](https://doi.org/10.1086/592324)
- Read, J. I., Hayfield, T., & Agertz, O. 2010, *Monthly Notices of the Royal Astronomical Society*, no–no, doi: [10.1111/j.1365-2966.2010.16577.x](https://doi.org/10.1111/j.1365-2966.2010.16577.x)
- Roediger, E., Kraft, R. P., Nulsen, P., et al. 2013, *Monthly Notices of the Royal Astronomical Society*, 436, 1721, doi: [10.1093/mnras/stt1691](https://doi.org/10.1093/mnras/stt1691)
- Roediger, E., & ZuHone, J. A. 2011, *Monthly Notices of the Royal Astronomical Society*, 419, 1338, doi: [10.1111/j.1365-2966.2011.19794.x](https://doi.org/10.1111/j.1365-2966.2011.19794.x)
- Roediger, E., Kraft, R. P., Nulsen, P. E. J., et al. 2015, *The Astrophysical Journal*, 806, 104, doi: [10.1088/0004-637x/806/1/104](https://doi.org/10.1088/0004-637x/806/1/104)
- Ruszkowski, M., Lee, D., Brügggen, M., Parrish, I., & Oh, S. P. 2011, *The Astrophysical Journal*, 740, 81, doi: [10.1088/0004-637x/740/2/81](https://doi.org/10.1088/0004-637x/740/2/81)
- Sanders, J. S., & Fabian, A. C. 2012, *Monthly Notices of the Royal Astronomical Society*, 421, 726, doi: [10.1111/j.1365-2966.2011.20348.x](https://doi.org/10.1111/j.1365-2966.2011.20348.x)
- Sarazin, C. L. 1986, *Rev. Mod. Phys.*, 58, 1, doi: [10.1103/RevModPhys.58.1](https://doi.org/10.1103/RevModPhys.58.1)
- Scannapieco, E., & Brügggen, M. 2008, *The Astrophysical Journal*, 686, 927, doi: [10.1086/591228](https://doi.org/10.1086/591228)
- Schekochihin, A. A., & Cowley, S. C. 2006, *Physics of Plasmas*, 13, doi: [10.1063/1.2179053](https://doi.org/10.1063/1.2179053)
- Schuecker, P., Finoguenov, A., Miniati, F., Böhringer, H., & Briel, U. G. 2004, *A&A*, 426, 387, doi: [10.1051/0004-6361:20041039](https://doi.org/10.1051/0004-6361:20041039)
- Sijacki, D., & Springel, V. 2006, *Monthly Notices of the Royal Astronomical Society*, 371, 1025, doi: [10.1111/j.1365-2966.2006.10752.x](https://doi.org/10.1111/j.1365-2966.2006.10752.x)
- Simonte, M., Vazza, F., Brighenti, F., et al. 2022, *A&A*, 658, A149, doi: [10.1051/0004-6361/202141703](https://doi.org/10.1051/0004-6361/202141703)
- Soltan, A., & Fabricant, D. G. 1990, *ApJ*, 364, 433, doi: [10.1086/169427](https://doi.org/10.1086/169427)
- Spitzer, L. 1962, *Physics of Fully Ionized Gases*
- Springel, V. 2005, *Monthly Notices of the Royal Astronomical Society*, 364, 1105, doi: [10.1111/j.1365-2966.2005.09655.x](https://doi.org/10.1111/j.1365-2966.2005.09655.x)
- Squire, J., Kunz, M., Arzamasskiy, L., et al. 2023, *Journal of Plasma Physics*, 89, 905890417, doi: [10.1017/S0022377823000727](https://doi.org/10.1017/S0022377823000727)
- Staszczyn, F. A., Dolag, K., & Beck, A. M. 2013, *MNRAS*, 428, 13, doi: [10.1093/mnras/sts018](https://doi.org/10.1093/mnras/sts018)
- Steinwandel, U. P., Böss, L. M., Dolag, K., & Lesch, H. 2022, *The Astrophysical Journal*, 933, 131, doi: [10.3847/1538-4357/ac715c](https://doi.org/10.3847/1538-4357/ac715c)
- Steinwandel, U. P., Dolag, K., Böss, L. M., & Marin-Gilabert, T. 2024, *The Astrophysical Journal*, 967, 125, doi: [10.3847/1538-4357/ad39ee](https://doi.org/10.3847/1538-4357/ad39ee)
- Su, K.-Y., Hopkins, P. F., Hayward, C. C., et al. 2017, *Monthly Notices of the Royal Astronomical Society*, 471, 144–166, doi: [10.1093/mnras/stx1463](https://doi.org/10.1093/mnras/stx1463)
- Suzuki, K., Ogawa, T., Matsumoto, Y., & Matsumoto, R. 2013, *The Astrophysical Journal*, 768, 175, doi: [10.1088/0004-637X/768/2/175](https://doi.org/10.1088/0004-637X/768/2/175)
- Teyssier, R., Moore, B., Martizzi, D., Dubois, Y., & Mayer, L. 2011, *Monthly Notices of the Royal Astronomical Society*, 414, 195–208, doi: [10.1111/j.1365-2966.2011.18399.x](https://doi.org/10.1111/j.1365-2966.2011.18399.x)
- Tormen, G., Bouchet, F. R., & White, S. D. M. 1997, *Monthly Notices of the Royal Astronomical Society*, 286, 865–884, doi: [10.1093/mnras/286.4.865](https://doi.org/10.1093/mnras/286.4.865)
- Tricco, T., & Price, D. 2013, *A Switch for Artificial Resistivity and Other Dissipation Terms.* <https://arxiv.org/abs/1310.4260>

- Valentini, M., & Brighenti, F. 2015, *MNRAS*, 448, 1979, doi: [10.1093/mnras/stv090](https://doi.org/10.1093/mnras/stv090)
- Vallés-Pérez, D., Planelles, S., & Quilis, V. 2021a, *Monthly Notices of the Royal Astronomical Society*, 504, 510–527, doi: [10.1093/mnras/stab880](https://doi.org/10.1093/mnras/stab880)
- . 2021b, *Computer Physics Communications*, 263, 107892, doi: [10.1016/j.cpc.2021.107892](https://doi.org/10.1016/j.cpc.2021.107892)
- Vallés-Pérez, D., Planelles, S., Quilis, V., et al. 2024, *Computer Physics Communications*, 304, 109305, doi: <https://doi.org/10.1016/j.cpc.2024.109305>
- Vazza, F., Jones, T. W., Brügggen, M., et al. 2016, *Monthly Notices of the Royal Astronomical Society*, 464, 210–230, doi: [10.1093/mnras/stw2351](https://doi.org/10.1093/mnras/stw2351)
- Wendland, H. 1995, *Advances in Computational Mathematics*, 4, 389
- XRISM Science Team. 2020, arXiv e-prints, arXiv:2003.04962, doi: [10.48550/arXiv.2003.04962](https://doi.org/10.48550/arXiv.2003.04962)
- Zeldovich, Y., & Raizer, Y. P. 1967, *Physics of Shock Waves and High Temperature Hydrodynamic Phenomena* (Academic Press), doi: [10.1016/B978-0-12-395672-9.X5001-2](https://doi.org/10.1016/B978-0-12-395672-9.X5001-2)
- Zhang, C., Churazov, E., Dolag, K., Forman, W. R., & Zhuravleva, I. 2020, *Monthly Notices of the Royal Astronomical Society*, 494, 4539, doi: [10.1093/mnras/staa1013](https://doi.org/10.1093/mnras/staa1013)
- Zhuravleva, I., Chen, M. C., Churazov, E., et al. 2023, *Monthly Notices of the Royal Astronomical Society*, 520, 5157–5172, doi: [10.1093/mnras/stad470](https://doi.org/10.1093/mnras/stad470)
- Zhuravleva, I., Churazov, E., Kravtsov, A., et al. 2012, *Monthly Notices of the Royal Astronomical Society*, 428, 3274–3287, doi: [10.1093/mnras/sts275](https://doi.org/10.1093/mnras/sts275)
- Zhuravleva, I., Churazov, E., Schekochihin, A. A., et al. 2019, *Nature Astronomy*, 3, 832–837, doi: [10.1038/s41550-019-0794-z](https://doi.org/10.1038/s41550-019-0794-z)
- Zhuravleva, I., Churazov, E. M., Schekochihin, A. A., et al. 2014, *The Astrophysical Journal*, 788, L13, doi: [10.1088/2041-8205/788/1/113](https://doi.org/10.1088/2041-8205/788/1/113)
- ZuHone, J. A. 2011, *The Astrophysical Journal*, 728, 54, doi: [10.1088/0004-637X/728/1/54](https://doi.org/10.1088/0004-637X/728/1/54)
- ZuHone, J. A., Kunz, M. W., Markevitch, M., Stone, J. M., & Biffi, V. 2015, *Astrophysical Journal*, 798, 90, doi: [10.1088/0004-637X/798/2/90](https://doi.org/10.1088/0004-637X/798/2/90)
- ZuHone, J. A., Lamb, D. Q., & Ricker, P. M. 2009, *The Astrophysical Journal*, 696, 694, doi: [10.1088/0004-637X/696/1/694](https://doi.org/10.1088/0004-637X/696/1/694)